



DEGREE PROJECT IN FLUID MECHANICS,
SECOND CYCLE, 30 CREDITS
STOCKHOLM, SWEDEN 2024

Design and optimization of a pulsed power generator for electrical wire explosion

Francesc Hernández Garcia

Author

Francesc Hernández Garcia <fhg@kth.se>
Master's Programme, Aerospace Engineering, 120 credits
KTH Royal Institute of Technology

Main Supervisor & Examiner

Prof. Michael Liverts <liverts@kth.se>
Department of Engineering Mechanics
KTH Royal Institute of Technology

Co-supervisor

Post-doc. Sebastián Rojas Mata <serm@kth.se>
Department of Engineering Mechanics
KTH Royal Institute of Technology

Place for Project

Stockholm, Sweden
Fluid Physics Laboratory

Date: June, 2024

Contents

I	Introduction	2
I-A	Problem Definition	2
I-B	Project Drivers and Future Applications	2
I-C	Aim and Scope of the Project	2
I-D	Delimitations	3
I-E	Benefits, Ethics and Sustainability	3
I-F	Outline	3
II	State of the Art	3
II-A	The Search of a Blast Wave Self-Similar Solution	3
II-B	Energy Partition During Exploding Wire Phenomena	5
II-C	Effect of the Circuit Parameters on the Explosion Properties	6
III	Theoretical Background	7
III-A	Transient Second-Order RLC Circuits	7
III-A1	Constitutive Laws	7
III-A2	Waveform Equations	7
III-B	Schlieren and Shadowgraph Techniques	8
III-B1	Ray Deflection Through Inhomogeneous Media	8
III-B2	Differences between Shadograph and Schlieren	8
III-B3	The Z-type Mirror System	9
III-C	Conservation Equations for Inviscid Flows	9
III-D	One-Dimensional Normal Shock Wave Relations	10
III-D1	Normal Shock Waves in a Perfect Gas	10
III-D2	Normal Shock Waves in Water	11
III-E	Exploding Wire Magnetohydrodynamics	11
IV	Methods	12
IV-A	Pulsed Power Generator	12
IV-B	System Connections	13
IV-C	Optical Setup	14
IV-D	Explosion Procedure and Safety Considerations	15
V	Results	16
V-A	Electrical Characterization of the PPG	16
V-A1	Short Circuit Experimental Results	16
V-A2	Analytical Model Analogy	16
V-A3	Numerical Model Simulation	18
V-A4	Comparison of the Models	18
V-B	Shock Wave Generation	19
V-B1	Video Analysis of the Shock Wave Position	19
V-B2	Analysis of the Electrical Waveforms	20
V-B3	Electrical Energy Transferred to the Wire	21
V-B4	Mechanical Energy Transferred to the Shock Wave	24
V-B5	Electrical-to-Mechanical Energy Conversion	25
VI	Discussion	26
VI-A	Existence of an Optimal Wire Diameter	26
VI-B	Applicability of Theoretical and CFD Models	27
VII	Conclusion	28
VII-A	Summary	28
VII-B	Future Work	29
	References	31

Design and optimization of a pulsed power generator for electrical wire explosion

MScAE Francesc Hernández García

Abstract—This master’s thesis aims to develop robust techniques for inducing extreme conditions in fluids by employing a Pulsed Power Generator (PPG). The project focuses on studying and controlling electrically induced single-wire explosions to efficiently produce shock waves in air and water. An in-depth literature review is conducted, followed by an exploration of the necessary theoretical background to understand the multidisciplinary physical phenomena. A methodology is developed to ensure the safe operation of the PPG, along with defining the Schlieren optical setup and operating procedures for the high-speed camera capable of reaching rates up to 10 million frames per second. The electrical parameters of the PPG are determined through short-circuit experiments and compared to an analogous RLC-like circuit using analytical and numerical simulations. Systematic experimentation is conducted across different copper wire diameters of $\varnothing 150\ \mu\text{m}$, $\varnothing 400\ \mu\text{m}$ and $\varnothing 500\ \mu\text{m}$ and different initial capacitor voltages up to 23 kV. The optimal explosion conditions are identified, notably with a wire diameter of $\varnothing 400\ \mu\text{m}$ in air, resulting in peak pressures in the order of hundreds of bar and Mach numbers up to 21.4. In water, the peak pressures reach tens of kilobar and Mach numbers up to 1.8. The analysis quantifies the transferred electrical energy and initial mechanical energy of the shock waves, reaching power magnitudes in the order of gigawatts and electrical-to-mechanical energy transfer efficiency up to 34%. The results are compared with numerical simulations and existing literature, culminating in a comprehensive report that synthesizes findings from literature review, hands-on experimentation, and analysis.

Sammanfattning—Denna masteruppsats syftar till att utveckla robusta tekniker för att inducera extrema förhållanden i fluida med hjälp av en Pulserande Kraftgenerator (PPG). Projektet fokuserar på att studera och kontrollera elektriskt inducerade explosionsfenomen med en enda tråd för att effektivt producera stötvågor i luft och vatten. En grundlig litteraturoversikt genomförs, följt av en utforskning av den nödvändiga teoretiska bakgrunden för att förstå de mångdisciplinära fysikaliska fenomenen. En metodik utvecklas för att säkerställa säker drift av PPG, tillsammans med definieringen av det Schlieren-optiska uppställningen och driftsförfarandena för höghastighetskameran som kan nå hastigheter på upp till 10 miljoner bilder per sekund. De elektriska parametrarna för PPG bestäms genom kortslutningsexperiment och jämförs med en analog RLC-liknande krets med analytiska och numeriska simuleringar. Systematiska experiment utförs med olika koppartråddiametrar på $\varnothing 150\ \mu\text{m}$, $\varnothing 400\ \mu\text{m}$ och $\varnothing 500\ \mu\text{m}$ och olika initiala kondensatorspänningar upp till 23 kV. De optimala explosionsförhållandena identifieras, särskilt med en tråddiameter på $\varnothing 400\ \mu\text{m}$ i luft, vilket resulterar i topptryck på ordningen hundratals bar och Mach-nummer upp till 21.4. I vatten når topptrycken tiotals kilobar och Mach-nummer upp till 1.8. Analysen kvantifierar den överförda elektriska energin och den initiala mekaniska energin hos stötvågorna, vilket når effektmagnituder på ordningen gigawatt och en överföringseffektivitet av elektrisk till mekanisk energi på upp till 34%. Resultaten jämförs med numeriska simuleringar och befintlig litteratur, vilket kulminerar i en omfattande rapport som sammanfattar resultaten från litteraturgenomgången, praktisk experimentation och analys.

Index Terms—Pulsed Power Generator, Electrically Induced Wire Explosion, Shock Wave Generation, Compressible Fluid Dynamics, High Voltage Engineering.

NOMENCLATURE AND ACRONYMS

R	Resistance [Ω]
L	Inductance [H]
C	Capacitance [F]
i	Current [A]
v	Voltage [V]
ε	Dielectric permittivity [F/m]
μ	Magnetic permeability [H/m]
σ	Electrical conductivity [S/m]
D	Diameter [m]
l	Length [m]
s	Laplace variable
ρ	Density [kg/m^3] or Electrical resistivity [$\Omega\cdot\text{m}$]
\mathbf{V}	Velocity vector (u, v, w) [m/s]
p	Pressure [Pa]
T	Temperature [K]
h	Specific enthalpy [J/kg]
e	Specific internal energy [J/kg]
a	Speed of sound [m/s]
γ	Ratio of specific heats
\dot{q}	Heat addition rate [W/kg]
\mathbf{f}	Body forces vector (f_x, f_y, f_z) [N/kg]
M	Mach number
W	Shock wave speed [m/s]
u_p	Speed of particles behind the shock [m/s]

<i>AUFS</i>	Artificial Upstream Flux Vector Splitting
<i>CFD</i>	Computational Fluid Dynamics
<i>CS</i>	Contact Surface
<i>EOS</i>	Equation Of State
<i>EWE</i>	Electrical Wire Explosion
<i>FPL</i>	Fluid Physics Laboratory
<i>FVM</i>	Finite Volume Method
<i>KCL</i>	Kirchhoff’s Current Law
<i>KTH</i>	Kungliga Tekniska Högskolan
<i>LHS</i>	Left-Hand Side
<i>MHD</i>	Magnetohydrodynamics
<i>PPG</i>	Pulsed Power Generator
<i>RC</i>	Rogowski Coil
<i>RHS</i>	Right-Hand Side
<i>SW</i>	Shock Wave
<i>SWG</i>	Shock Wave Group
<i>TDT</i>	Total Damping Time
<i>UPS</i>	Uninterruptible Power Supply

I. INTRODUCTION

DELVING into shock wave generation is a fascinating exploration bridging physics, engineering, and applied sciences. In this field, cutting-edge technologies like the Pulsed Power Generator (PPG) take centre stage, offering a more adaptable and precisely controllable means of generating extreme conditions in fluids compared to traditional methods such as shock tubes.

The significance of exploring shock wave generation extends to both diverging and converging phenomena. Diverging shock waves, characterized by rapid outward expansion, are central to this investigation. This thesis primarily handles the controlled generation and manipulation of explosive diverging shock waves using a PPG. The PPG discharges a huge current through a thin wire, which heats up and changes its phase rapidly from solid-to-liquid, liquid-to-gas and gas-to-plasma, expanding abruptly to create a shock wave in the surrounding medium. This process is called Electrical Wire Explosion (EWE).

Understanding converging shock waves, characterized by their rapid inward collapse, is likewise considered important within the scientific community due to its multiple applications. In astrophysics, these implosions are analogous to the shock waves produced by the implosion of massive stars, influencing the dynamics of galaxies. Replicating the phenomena achieved by cosmic events in the lab using PPGs uncovers the fundamental physics behind star processes [1]. The relevance of generating imploding shock waves extends to nuclear fusion research. PPGs play a pivotal role here, using shock waves to compress and heat fusion fuel, mimicking the extreme conditions needed for nuclear fusion reactions [2]. The controlled implosion achieved through pulsed power technology is vital for advancing in fusion research, offering potential breakthroughs in clean and sustainable energy production.

The following master's thesis dives deeper into the functioning of a PPG. Its electrical mechanisms will be examined to assess its efficiency in creating shock waves through electrically induced wire explosions. A deeper understanding of the underlying processes and forces involved will be sought through careful examination of these single-wire explosions. This knowledge is considered key to unlocking the PPG's full potential for even more complex and groundbreaking experiments in the future. By gaining insights into the PPG's operation, the future goal is to achieve a more comprehensive understanding of shock wave generation and the development of innovative applications across various scientific disciplines.

A. Problem Definition

A PPG is a system able to create a strong and fast discharge of electrical energy through a very thin wire, producing a controlled explosion followed by a shock wave in the surrounding medium. The discharge is typically in the range of hundreds of kiloamperes and lasts for less than a microsecond. By the

establishment of an experimental facility using one of these systems in the Fluid Physics Laboratory (FPL) of the Kungliga Tekniska Högskolan (KTH), the following research question is formulated:

How do we determine the optimized PPG parameters and initial conditions seeking for the most efficient electrical-to-mechanical energy transformation?

B. Project Drivers and Future Applications

The main driver of this project is being able to generate single-wire explosive diverging shock waves with a PPG in an efficient and controllable manner. This is carried out at the new PPG machine recently acquired by the researchers in the Shock Wave Group (SWG) of the FPL, within the context of the ERC-funded DYNPRESS project. The performance of the machine was still to be characterized at the beginning of this work, hence the relevance of this thesis in which the first explosions of the machine have been carried out. While the immediate objective has been to analyze and encapsulate the behaviour of the PPG, the long-term aim of the research group is to induce highly extreme conditions in various materials through diverse means.

An immediate future application of this work is to use the PPG for shock-focusing. This type of work is actively being carried out by this research group utilising a shock tube. While a shock tube is highly reliable and controllable, it may be more limited in reaching extreme conditions compared to a PPG. Previous research on this topic was conducted by Michael Liverts and Nicholas Apazidis in their 2016 paper [3]. A second immediate future application is to explore the generation of shock waves in different gases, liquids and solids. The PPG offers high versatility in terms of changing the working medium, for which is an ideal tool to study how extreme conditions are achieved in different materials. Previous work on this topic has been carried out by D. Yanuka et al. in their 2019 paper [4], where they achieve pressures in the order of tens of GPa in different mediums.

C. Aim and Scope of the Project

This project aims to develop techniques to use the PPG for shock wave generation in air and water. More concretely, the scope consists of the following ten tasks:

- (i) Perform a literature review of advances in exploding wires employing a PPG and summarize the state of the art.
- (ii) Understand and summarize the multidisciplinary theoretical background involving the PPG operation and shock wave generation through EWE.
- (iii) Describe the methodology involving the operation of the PPG, the functioning of the system and the optical setup. Create a standardized explosion procedure for the safe operation of the system.

- (iv) Determine the electrical parameters of the PPG by using experimental measurements of voltage and current in short-circuit experiments. Validate the results with analytical models and simulations.
- (v) Calibrate a Rogowski Coil (RC) used for current measurement and find relations between the different high-voltage probes employed in the experiments.
- (vi) Explode wires of different diameters in air and water in a systematic experimental campaign. Record the electrical waveforms and the shock wave expansion videos for further analysis.
- (vii) Calculate the electrical energy transferred to the wire until the moment of the explosion for different wire diameters. Estimate the mechanical energy transferred to the shock wave.
- (viii) Study the electrical-to-mechanical energy conversion by studying the strength of the generated shock waves for different diameters and mediums.
- (ix) Discuss the shock wave behaviour and compare it to strong shock wave theory and simulations, performing two-dimensional Computational Fluid Dynamics (CFD) simulations of the wire explosions in air.
- (x) Summarize the obtained results and analyse the possible future work to develop after this thesis.

D. Delimitations

This section states the delimitations of the project, referring to the boundaries or limitations that define the scope and experiments. The project treats divergent shock waves generated by single-wire explosions. Although shock focusing is of high scientific interest, it will not be handled in this thesis. Only two different fluid mediums are studied: air and water. The project does not include any invasive or non-invasive pressure measurements on the test medium. The explosions are recorded at the very vicinity of the centre axis of the wire, in a radial range of a maximum length of 3 cm. The thesis does not include a study on the effect of the length of the wires in the generated shock waves, although it is assessed conceptually. All the wires have a length of $l = 6$ cm and are made out of copper. Only three different wire diameters are studied: $\varnothing 150 \mu\text{m}$, $\varnothing 400 \mu\text{m}$ and $\varnothing 500 \mu\text{m}$. The plasma resulting from the explosions is not characterized. No magnetohydrodynamics (MHD) simulations are included, although their underlying physics is studied in the theoretical background. The effect of possible cavitation or turbulence after the explosion is not studied.

E. Benefits, Ethics and Sustainability

The study of shock wave generation using advanced technologies like the PPG presents numerous benefits across various scientific and practical fields. By delving into methods for shock wave generation, this research contributes to advancing

the understanding of fundamental physics principles governing extreme conditions. Such insights have important implications in different disciplines, ranging from astrophysical phenomena to nuclear fusion research. The PPG can also be utilized in various industrial applications beyond shock wave generation, including food processing, medical treatment, water treatment, exhaust gas treatment, ozone generation, engine ignition, ion implantation, and more [5].

Ethically, this research pursues the responsible and safe conduct of experiments involving high-voltage engineering. Measures are taken to mitigate risks associated with experimental procedures, ensuring the well-being of researchers and maintaining environmental sustainability. In terms of sustainability, while the pursuit of scientific knowledge often involves resource-intensive experiments, efforts are made to minimize environmental impact and promote sustainable practices wherever possible. This includes responsible waste management, energy-efficient laboratory protocols, and consideration of the broader ecological implications of research activities.

F. Outline

The outline of this master's thesis project consists of the following: a literature review in the form of state of the art given in Section II; a summary of the relevant theoretical background in Section III; a description of the employed methods and methodology in Section IV; a summary of the obtained results from the experiments in Section V; a discussion of the obtained results including theoretical analysis and simulations in Section VI; and a conclusion summarizing the thesis and emphasizing future work in Section VII.

II. STATE OF THE ART

The phenomenon of exploding wires has captivated researchers for decades. This review delves into the interplay between theoretical predictions and experimental observations in this domain. This section embarks on a chronological journey through several authors, exploring the physical principles governing cylindrical blast waves and their connection to exploding wire phenomena.

A. The Search of a Blast Wave Self-Similar Solution

In 1954, Shao-Chi Lin's [6] groundbreaking paper laid the foundation for analyzing cylindrical blast waves. A blast wave is a shock wave followed very rapidly by an expansion. Inspired by G. I. Taylor's work on spherical explosions [7], Lin extended the concepts to cylindrical geometry. The core assumption was that a significant amount of energy per unit length, denoted by E , is instantaneously released along a straight path in a gaseous atmosphere. This sudden energy input triggers a powerful cylindrical shock wave that propagates outward with time. Lin's analysis relied on the concept of similarity solutions. Imagine a cylindrical shock wave expanding in a gas. At any given time, the pressure p ,

density ρ , and velocity u of the gas can be expressed in terms of a single similarity parameter η that depends on the distance from the source R and time t . This approach simplifies the complex governing equations into a more manageable form suitable for solving the problem.

One of the key findings of Lin's work was the relationship between the shock wave radius R and time t . He derived equation (1), where $S(\gamma)$ is a parameter that depends on the heat capacity ratio of the gas γ , yielding $S(\gamma) = 1.009$ for air. This equation is also known as Sedov's equation. As a consequence of it, the peak pressure immediately behind the blast wave can be computed with equation (2).

$$R(t) = S(\gamma) \cdot (E/\rho_0)^{1/4} t^{1/2}, \quad (1)$$

$$p = 0.216 \cdot E/R^2. \quad (2)$$

This equation relates the pressure behind the shock wave to the distance travelled, indicating a pressure decay with an inverse square dependence on the radius. This means that as the shock wave propagates outward (R increases), the pressure behind the wavefront weakens. However, limitations existed in Lin's work due to simplifying assumptions. The constant specific heat assumption, while offering a tractable analysis, deviates from reality at high temperatures encountered in explosions. The instantaneous energy deposition is generally an over-simplification. Despite these limitations, Lin's work provided a valuable starting point for understanding the behaviour of cylindrical blast waves.

Bennett's 1958 paper [8] marked a significant advancement by introducing an experimental technique to visualize the cylindrical shock wave produced by exploding wires. This technique allowed Bennett to capture clear outlines of the parabolic shock wave as it propagated ahead of the luminous Contact Surface (CS), the region of intense light emission associated with the surface separating the wire and surrounding medium. The separation of the shock wave and the CS was observed to occur within a microsecond, highlighting their distinct characteristics. By comparing the observed shock wave trajectories with predictions from Lin's similarity solutions, Bennett found evidence suggesting that the shock wave might receive additional energy during the early stages of its propagation. However, after this initial phase, both the shock wave and the CS exhibited a parabolic growth pattern consistent with the theoretical predictions. Bennett's work not only validated the usefulness of shock wave visualization but also emphasized the importance of distinguishing between the shock wave and the CS in analyzing exploding wire phenomena. He pointed out that previous streak camera data likely captured primarily the CS luminosities, neglecting the crucial role of the shock wave.

Oshima's work in 1962 [9] delved deeper into the experimental characterization of cylindrical blast waves generated by exploding wires. To achieve strong blast waves, he recognized the limitations of using standard atmospheric pressure. Air at ambient pressure offers relatively significant resistance to

the expanding shock wave, leading to a weaker blast with a rapidly decaying pressure profile. To address this, Oshima conducted his experiments in a shock chamber evacuated to various low pressures. This reduced air density offered less resistance to the initial energy deposition, allowing the blast wave to grow stronger and propagate further before significant weakening occurred. To probe the internal structure of the blast wave, Oshima employed a Mach-Zehnder interferometer. This instrument utilizes the interference of light waves to measure variations in the refractive index of a medium. In the context of the blast wave, these variations correspond to changes in the gas density within the wave. By analyzing the interferometer data, Oshima could reconstruct the density distribution across the blast wave. This detailed information allowed for a more comprehensive understanding of the wave's internal structure compared to just measuring the shock wave front's position and arrival time. The good agreement between Oshima's experimental results and the theoretical predictions validated the underlying physical principles governing cylindrical blast waves. He concluded that performing explosions at low ambient pressures increases the matching with the theoretical predictions.

In the same year, Bennett and Shear [10] performed experiments at very low ambient density conditions, observing important deviations from the $\rho_0^{-1/4}$ dependence of shock front predicted by Lin's equation (1). For ambient pressures $p \geq 1/2$ atm, the formation of shock waves by exploding wires is successfully accounted for by Lin's equation, as Oshima also observed. For even lower pressures $p \leq 1/4$ atm, the deviations from the blast wave theory start being relevant. They associate this behaviour with the mechanism of generation of the shock wave. It is argued that the appearance and development of transient plasma over the wire is caused by a peripheral arc. According to them, the shock wave would be mainly generated by the expansion of this arc plasma rather than by the expansion of the wire, which would also contribute to the energy of the shock wave in a non-dominant way.

Sakurai's 1964 paper [11] provided a broader theoretical framework for analyzing blast waves generated by various sources, including exploding wires. He introduced a method for finding approximate solutions for an idealized model where the gas-dynamic motion is initiated by an instantaneous energy release from a point source (spherical), line source (cylindrical), or plane source. The key concept in Sakurai's approach is the use of similarity transformations. By introducing a similarity parameter, the governing equations become more manageable for approximate solutions. These solutions are typically obtained through power series expansions, allowing for efficient calculations. Sakurai then addressed the applicability of blast wave theory to exploding wire phenomena. While the theory offers valuable insights, it is crucial to recognize the limitations and ensure the experimental conditions align with the assumptions embedded in the theory.

The theory holds for a specific spatial region where the fundamental assumption of an instantaneous line source releasing energy is satisfied. This translates to a distance R from the

exploding wire that is significantly larger than the radius of a cylinder of air with a mass equivalent to the explosive material in the wire (denoted by \bar{R}). For instance, for a typical copper wire with a diameter of 0.1 mm at atmospheric pressure, \bar{R} is approximately 0.4 cm. Therefore, the theory would only be applicable in the region where $R \gg \bar{R}$, which implies that R must exceed 4 cm or similar. Data from regions closer to the exploding wire ($R < 4$ cm) would likely deviate from theoretical predictions. On the other hand, the theory also limits R to be significantly smaller than a magnitude R_0 , which is given in equation (3).

$$R_0 = \left(\frac{E}{2\pi p_0} \right)^{1/2} \quad (3)$$

Note that E is expected to be in the range of 5–100 J/cm, which for atmospheric pressure would give typical values of R_0 between 2.8–12.6 cm. More concretely, Sakurai defines $R \leq 0.4R_0$ as the limit for the applicability of the theoretical solution. Therefore, the theoretical approach will be valid in the region $R \gg \bar{R}$ and $R \leq 0.4R_0$, which might not exist at all. Note that by decreasing p_0 , the theoretical predictions will be more similar to the experimental results, as Oshima observed in his 1962 paper. The theory relies on the strong shock wave assumption, which neglects higher-order terms in the analysis for simplicity. This translates to a proportionality between the squared distance travelled R^2 and time t for the shock wave propagation. However, experimental observations often reveal a better fit with a relationship of $R^{5/3}$ and time t . This discrepancy suggests that the energy input from the exploding wire might not be instantaneous but occurs over a short period, leading to a flow with energy addition. While the theory can be extended to account for such energy addition, it becomes more complex.

B. Energy Partition During Exploding Wire Phenomena

Understanding the energy partition within the exploding wire is crucial for optimizing its applications. This analysis delves into three key papers that explore this concept, focusing on the interplay between electrical behaviour and the resulting mechanical effects, with an emphasis on how it affects the efficiency of shock wave generation.

Bennett's 1958 work [12], investigates the energy distribution within the exploding wire by analyzing the circuit's damping time. The study employs streak camera data and analyzes the energy associated with the shock wave and the CS. A key finding is the existence of an optimum wire diameter for a given length that maximizes the specific shock wave energy. However, this observation deviates from the minimum observed in the total damping time (TDT) of the circuit. Bennett attributes this discrepancy to the presence of residual circuit resistance, which impacts the overall energy transfer. This implies that the exploding wire exhibits non-ideal behaviour compared to the theoretical model of instantaneous line source energy release. Bennett's work emphasizes the need for further investigation into the factors influencing

the energy partition within the exploding wire, particularly the role of non-idealities in the circuit.

P. V. Phung and D. O. Miles [13] address the role of the skin effect in their 1975 paper. The skin effect describes the tendency of high-frequency currents to concentrate near the conductor's surface. In exploding wires, this phenomenon becomes relevant due to the rapid rise in current during the explosion. The skin depth is the characteristic depth at which the current density falls to $1/e$ (approximately 37%) of its surface value. At high frequencies, the current tends to concentrate in the outer layers of the conductor, with minimal penetration into the core. The paper develops a method for calculating the current density distribution within a cylindrical conductor under such fast-pulse, high-current conditions. They consider the dependence of the conductor's resistivity on temperature due to the extensive Joule heating experienced during the explosion. Their analysis reveals that the current density is not uniform throughout the wire's cross-section. Initially, the current concentrates near the surface due to the skin effect. As the explosion progresses, the current diffuses inwards, eventually leading to a more uniform distribution. This non-uniform current distribution has significant consequences for energy partition within the exploding wire.

Gonzalo Rodríguez Prieto et al. [14] in their 2016 work experimentally investigate the energy transfer dynamics in an exploding wire system. They analyze both the plasma dynamics and the electrical energy delivered by the circuit to the wire. Through visible light streak images, they observe the radial expansion of the plasma generated during the explosion. Simultaneously, the voltage and current traces of the circuit are analyzed to understand the temporal distribution of the electrical energy transfer. A significant finding is that a substantial portion of the electrical energy is transferred to the exploding wire even during the plasma expansion phase. Furthermore, lower limits for the resistivity during this expansion suggest the presence of a central metallic core, either liquid or solid, alongside the expanding plasma. This yields the conclusion that the wire surface is the first part of the wire suffering ablation due to the skin depth effect, as it is illustrated in Figure 1. The centre of the wire may remain in solid state even after the generation of the shock wave by the expanding plasma closer to the surface.

The insights from these three papers collectively paint a clearer picture of the energy partition within an exploding wire and how it affects the efficiency of shock wave generation. Bennett's work establishes the existence of non-ideal behaviour, with the skin effect playing a crucial role as highlighted by Phung and Miles and Gonzalo Rodríguez Prieto et al. This has two key consequences for energy partition: (1) the surface region experiences more intense Joule heating compared to the core. This leads to a non-uniform distribution of thermal energy within the wire; and (2) the current diffusion process takes time, resulting in a delay in transferring the full electrical energy stored in the capacitor to the entire wire volume. These combined effects contribute to a less efficient conversion of electrical energy into the mechanical energy

associated with the shock wave. Energy is diverted towards heating the surface region more intensely, which may not contribute significantly to the shock wave generation. This decreases the mechanical energy of the generated shock wave.

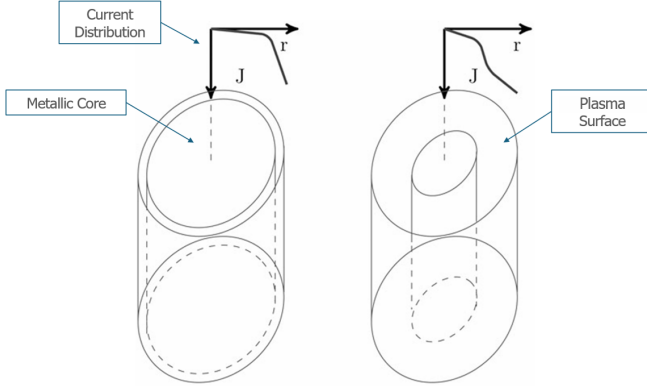


Fig. 1: Two consecutive stages of metallic wire ablation with the current density over-imposed [14].

C. Effect of the Circuit Parameters on the Explosion Properties

EWE is a phenomenon where a high-intensity current pulse rapidly heats a thin wire, causing it to vaporize and create a plasma plume. This process has numerous applications, including nanoparticle generation and shock wave formation. The properties of the resulting plasma and shock wave are highly dependent on the circuit parameters and wire properties used in the EWE setup. This section will review three key papers that explore this connection.

Qing Zhou et al. [15] in 2011 investigated the influence of circuit parameters (discharge voltage and circuit inductance) and wire properties (length and diameter) on the underwater electrical explosion of copper wires using microsecond timescale pulsed discharges. They measure the current and voltage waveforms to analyze the effect of the current rise rate on the phase transitions involved in the explosion process. As the current through the wire increases rapidly, its temperature rises due to Ohmic heating. This heating first leads to the melting of the solid copper wire (solid-to-liquid phase transition). Further increase in temperature causes the liquid copper to vaporize (liquid-to-vapor phase transition), creating a conducting plasma. The rate at which the current rises determines the speed of these phase transitions. The authors observed that increasing the discharge voltage or decreasing the circuit inductance accelerates the current rise rate. A faster current rise rate leads to faster heating and a more rapid explosion. This faster explosion process deposits more energy into the wire during vaporization compared to the melting and breakdown stages.

Additionally, increasing the wire length results in higher peak voltage but lower specific energy deposited before breakdown. This is because the longer wire has a higher resistance, requiring a higher voltage to achieve the same current. On the

other hand, increasing the wire diameter has a complex effect due to the skin depth effect. For thicker wires used in EWE experiments, the current may only flow through a thin outer layer due to this effect. This limits the amount of material effectively participating in the explosion and can lead to a slower and less energetic process compared to thinner wires, which can relate to the observations by Gonzalo Rodríguez Prieto et al. [14].

Kyoung-Jae Chung et al. [16] in 2016 present a one-dimensional MHD model to simulate the EWE process of copper wires in water. Their model incorporates a wide-range equation of state (EOS) and electrical conductivity data for copper to account for the material's behaviour across different phases (solid, liquid, plasma). This allows them to analyze the dynamics of the exploding wire and the generation of a shock wave in the surrounding water. The MHD equations describe the interaction between the electromagnetic field, fluid motion, and thermal energy within the exploding wire. The EOS relates the pressure, density, and temperature of the material, providing crucial information about its phase transitions. The electrical conductivity determines how readily the material conducts current, which is essential for understanding the Ohmic heating process.

The model successfully reproduces the experimental observations of wire explosion and shock wave formation. The rapid expansion of the vaporized wire generates a strong shock wave in the surrounding water. The model also captures the phenomenon of current dwell and restrike, where the current flow momentarily pauses before resuming. This behaviour is attributed to the cooling of the wire during the current dwell after a very rapid first expansion of the plasma, which reduces its conductivity and hinders current flow. Once the temperature rises again, the current can resume. While the model provides valuable insights, it highlights the limitations of neglecting radiation loss at high temperatures. When the wire temperature exceeds a certain threshold, radiation loss becomes significant and can affect the final temperature and energy distribution within the system.

Guofeng Yin et al. [17] in 2019 developed a coupled model that describes the circuit, the exploding wire, and the evolution of the shock wave generated during underwater EWE of copper wires. Their model utilizes wide-range EOS and conductivity data to simulate the process from the solid state. They investigate the influence of the discharge period on the peak pressure of the shock wave and the efficiency of energy conversion. The coupled model considers the interaction between the electrical circuit, the exploding wire, and the surrounding water, similarly to Chung's paper. The circuit parameters determine the current waveform delivered to the wire, which in turn governs the Ohmic heating and energy deposition.

The model successfully reproduces the experimental observations of current, voltage, wire radius evolution, and shock wave propagation. It highlights the dependence of the shock wave peak pressure on the initial wire diameter and the energy deposition process. A faster discharge (shorter

discharge period) tends to generate shock waves with higher initial peak pressure due to the rapid energy deposition into the wire. However, a slower discharge leads to shock waves with a slower radial attenuation (pressure decreasing slower with distance from the wire). The study also explores the efficiency of converting the deposited electrical energy into the mechanical energy of the shock wave. This efficiency is limited by factors such as radiation loss from the hot wire and energy dissipation during shock wave propagation. The model suggests that the efficiency typically ranges from 40% to 50% tens of microseconds after current initiation.

Faster current rise rates, achieved through higher discharge voltage or lower circuit inductance, lead to quicker heating, more rapid explosions, and a greater deposit of energy during vaporization. This emphasizes the importance of circuit parameters in influencing the explosion's characteristics by controlling the current rise rate. Wire diameter also plays a critical role due to the skin depth effect. While thicker wires might seem advantageous for absorbing more energy, the current tends to concentrate in the outer layers, limiting the amount of material actively participating in the explosion. Conversely, a thinner wire with a larger portion effectively heated can lead to a more energetic explosion.

III. THEORETICAL BACKGROUND

This section provides the necessary theoretical background to understand wire explosions using a PPG, the visualization techniques employed to record the phenomena, the conservation equations defining the fluid flow, and the behaviour of the generated shock waves.

A. Transient Second-Order RLC Circuits

Understanding the amount of energy transferred from the capacitors into the wire explosion requires an understanding of electrical transient second-order circuits. The PPG is simplified to an undriven series RLC circuit, where the initial voltage of the capacitors is the input to the system. All the information in this section is obtained from A. Agarwal and J.H. Lang [18]. Figure 2 shows a diagram of the RLC circuit employed as analogy for the PPG.

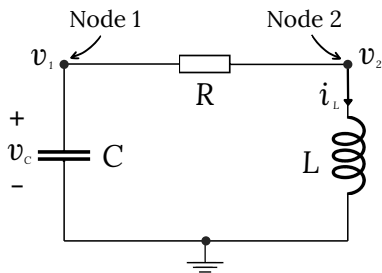


Fig. 2: Diagram of an undriven series RLC circuit.

1) *Constitutive Laws*: This subsection defines the constitutive laws for generic capacitors and inductors. Diagrams of both are included in Figure 3. For a capacitor with an insulating gap of height l and dielectric permittivity ϵ , each plate of the capacitor with area A gets charged with q when applied to a current. Following from Maxwell's equations, it is possible to find a relation between current and voltage in the capacitor, as defined in equation (4). Note that C is defined as the capacitance.

$$i(t) = C \frac{dv(t)}{dt}, \quad C = \frac{\epsilon A}{l}. \quad (4)$$

For an inductor with an insulator core having a magnetic permeability of μ , a conductor coil with a terminal on each end is wound with N turns around the toroidal core, covering a length l . The cross-sectional area of the coil around the core is A . Following from Maxwell's equations, it is possible to find a relation between current and voltage in the inductor, as defined in equation (5). Note that L is defined as the inductance.

$$v(t) = L \frac{di(t)}{dt}, \quad L = \frac{\mu N^2 A}{l}. \quad (5)$$

The stored energy of a charged capacitor is given by $E_C(t) = \frac{1}{2} C v_C(t)^2$, while for an inductor is $E_L(t) = \frac{1}{2} L i_L(t)^2$. These expressions will be relevant when computing the initial available energy in the PPG.

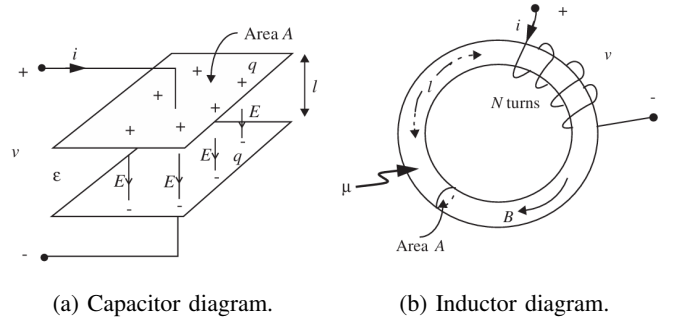


Fig. 3: Diagrams of a capacitor and inductor.

2) *Waveform Equations*: The RLC circuit defined in Figure 2 contains two main nodes. Here, Kirchoff's Current Law (KCL) is applied to Node #1 as given in equation (6), and to Node #2 as given in equation (7).

$$C \frac{dv_1}{dt} + \frac{v_1(t) - v_2(t)}{R} = 0 \quad (6)$$

$$\frac{v_2(t) - v_1(t)}{R} + \frac{1}{L} \int_{-\infty}^t v_2(\hat{t}) d\hat{t} = 0 \quad (7)$$

Note that the voltage at Node #1 is essentially the voltage difference in the capacitor $v_1(t) = v_C(t)$. Now, equations (6) and (7) are solved together for $v_1(t)$. Rearranging and differentiating, it is possible to find the following second-order

Ordinary Differential Equation (ODE) akin to a mass-spring-damper system, as given in equation (8).

$$\frac{d^2 v_C(t)}{dt^2} + \frac{R}{L} \frac{dv_C(t)}{dt} + \frac{1}{LC} v_C(t) = 0 \quad (8)$$

Equation (8) is a homogeneous linear ODE with constant coefficients. Since the system is undriven, the homogeneous solution is also its total solution. The solution is found by the superposition of two terms of the form Ae^{st} . Applying this substitution and simplifying, the left-hand side of equation (9) is given as the characteristic equation of the circuit.

$$s^2 + \frac{R}{L}s + \frac{1}{LC} = 0 \quad \longleftrightarrow \quad s^2 + 2\alpha s + \omega_0^2 = 0 \quad (9)$$

The two roots of this second-order polynomial are a function of α and ω_0 . These are given in equation 10 as a function of the circuit parameters R , L and C .

$$\alpha = \frac{R}{2L}, \quad \omega_0 = \frac{1}{\sqrt{LC}}. \quad (10)$$

Now, the solution for v_C is a linear combination of the two functions $A_1 e^{s_1 t}$ and $A_2 e^{s_2 t}$. The only remaining unknowns are A_1 and A_2 , which are completely determined by the initial conditions of the problem. In this case, the initial conditions are given by an initial capacitor voltage $v_C(0)$ and initial inductor current $i_L(0)$, which will be typically zero. The current can be found by applying the constitutive law of the capacitor defined in equation (4), noting that $i(t) = i_L(t) = i_C(t)$. Therefore, the waveform equations are given in equations (11) and (12).

$$v_C(t) = \frac{C s_2 v_C(0) + i_L(0)}{C(s_2 - s_1)} e^{s_1 t} + \frac{C s_1 v_C(0) + i_L(0)}{C(s_1 - s_2)} e^{s_2 t} \quad (11)$$

$$i_L(t) = -s_1 \frac{C s_2 v_C(0) + i_L(0)}{(s_2 - s_1)} e^{s_1 t} - s_2 \frac{C s_1 v_C(0) + i_L(0)}{(s_1 - s_2)} e^{s_2 t} \quad (12)$$

The formal analysis of the undriven RLC circuit for the given initial conditions is now complete. The behaviour of the system is determined by the relationship between α and ω_0 : if $\alpha < \omega_0$, it shows under-damped dynamics; if $\alpha = \omega_0$, it is critically damped; and if $\alpha > \omega_0$, it exhibits over-damped dynamics. Physically, under-damped dynamics in an RLC circuit involve oscillatory responses, critically damped dynamics result in a rapid but smooth return to equilibrium, and over-damped dynamics entail a sluggish response without oscillations.

The relative size between α and ω_0 is usually expressed in terms of the *Quality Factor* Q of the circuit, defined by $Q = \frac{\omega_0}{2\alpha} = \frac{1}{R} \sqrt{\frac{L}{C}}$. If the system is very under-damped, then Q will be large, and the system oscillates for a long time near the natural frequency. In the studied experiments, Q can be modified by changing the wire diameter and length, affecting the total resistance and inductance of the circuit. For

an under-damped system, the damped oscillation frequency of the system is $\omega_d = \sqrt{\omega_0^2 - \alpha^2}$. Therefore, the period of one oscillation is $2\pi/\omega_d$.

B. Schlieren and Shadowgraph Techniques

Wire explosions create powerful shock waves, invisible to the eye. Schlieren and Shadowgraph techniques, being non-intrusive, make these shock waves visible. This allows researchers to directly observe and analyze the characteristics of the shock wave, furthering our understanding of wire explosions and their applications. This section introduces basic concepts of the working mechanism of these techniques. Note that all the following information and graphs are extracted from Settles' book [19].

1) Ray Deflection Through Inhomogeneous Media: The refractive index of a transparent medium is a physical parameter that defines how fast electromagnetic waves can travel through a medium compared to vacuum. It is defined as $n = c_0/c$, where c_0 is the light speed in vacuum and c is the light speed in the medium. A change in the density of the medium will drive a change in its refractive index. For instance, for air and other gases, the refractive index changes with the gas density as $n - 1 = k\rho$, where $k \approx 0.23 \text{ cm}^3/\text{g}$ is the Gladstone-Dale coefficient at standard conditions. Therefore, changes in density will drive changes in the refractive index of the medium, and the light path will be deflected accordingly. Both Schlieren and Shadowgraph are visualization techniques that make use of these light deflections to capture density changes in images.

Therefore, it is crucial to understand how light is deflected when encountering a change in refraction index. It can be shown that a gradient in refractive index in an x,y-plane drives the following light deflections:

$$\frac{\partial^2 x}{\partial z^2} = \frac{1}{n} \frac{\partial n}{\partial x}, \quad \frac{\partial^2 y}{\partial z^2} = \frac{1}{n} \frac{\partial n}{\partial y}. \quad (13)$$

Equation (13) shows that light rays are always bent towards the region of high refractive index and density.

2) Differences between Shadograph and Schlieren: Schlieren and Shadowgraph methods, though related, have distinct characteristics. Shadowgrams are mere shadows created by the light ray deflection through an inhomogeneous media. Schlieren technique requires a cutoff of refracted light using a knife-edge, used to block out any indirect light from entering the system, while Shadowgraph does not. The illuminance level of Schlieren images responds to the first spatial derivative of the refractive index, while Shadowgraph responds to the second derivative. Both methods integrate line-of-sight information onto a viewing screen, suitable mainly for 2-D phenomena. Shadowgraph offers ease of use with minimal equipment, whereas Schlieren requires more elaborate setups. However, Schlieren stands out in sensitivity, particularly in capturing fine details and nuances. While Shadowgraph is

adept at visualizing large-scale phenomena, Schlieren is better suited for detecting subtle variations, making it advantageous in various applications.

3) *The Z-type Mirror System:* These visualization techniques have two types of systems: lens- and mirror-type. The choice between lens and mirror-based instruments hinges on a balance between simplicity, cost, and performance. Lens-based systems are easier to align. However, lenses suffer from chromatic aberration, causing color fringing in the image. This can be mitigated with filters but limits the size and increases the cost of large lenses. Mirrors, on the other hand, require a folded design which can be less convenient and difficult to align. Additionally, they can introduce off-axis aberrations like coma and astigmatism under certain conditions. Despite these drawbacks, mirrors are significantly cheaper, especially for larger systems, and only require one precisely polished surface compared to the multiple surfaces needed for lenses. Since mirrors also don't suffer from chromatic aberration, they usually become the preferred choice for large-scale Schlieren applications due to their cost-effectiveness and simpler manufacturing process.

In the laboratory arrangement employed to record the wire explosions for this thesis, a z-type-based Schlieren mirror system is employed. A sketch is included in Figure 4.

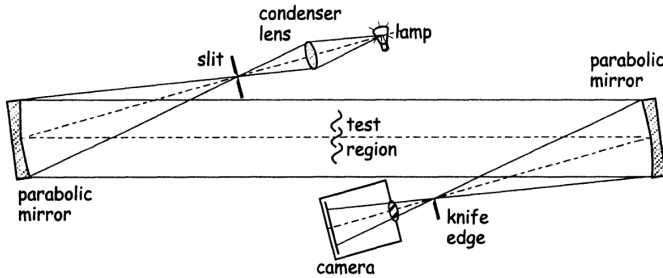


Fig. 4: Sketch of a z-type Schlieren arrangement [19].

This arrangement is called the Herscellian z-type system, which uses two-oppositely tilted, on-axis telescopic parabolas. It consists of a light source, typically a laser, that emits a light beam that will be redirected to the test region through a first parabolic mirror. The function of the slit is to make the light beam come from a point source, which enables the parabolic mirror to collimate better the light into a parallel beam. The slit is typically not necessary if the light source is a laser with a small optical fibre. The experiment is carried out in the test region, changing the density of the media and deflecting the light, which is redirected into the camera using a second parabolic mirror. The knife-edge is put between the second parabolic mirror and the camera, cutting off the refracted light. If the knife-edge is taken out, the system behaves like a Shadowgraph.

C. Conservation Equations for Inviscid Flows

This section summarizes the conservation equations describing the mass, momentum and energy of inviscid flows

in their integral and derivative forms. All the information regarding fluid mechanics is obtained from Anderson [20], unless otherwise specified. Understanding these equations is crucial for being able to solve any fluid mechanics problem, including the change in pressure, density and temperature over a shock wave. The first of these equations in their integral form is the continuity equation (14), which relates the mass flow rate over the surface of a control volume with the temporal derivative of the mass in the control volume.

$$-\oint_S \rho \mathbf{V} \cdot d\mathbf{S} = \frac{\partial}{\partial t} \iiint_V \rho dV \quad (14)$$

Note that V stands for the volume inside the domain, while S stands for its surface. The momentum equation in integral form is given in equation (15).

$$\oint_S (\rho \mathbf{V} \cdot d\mathbf{S}) \mathbf{V} + \iiint_V \frac{\partial (\rho \mathbf{V})}{\partial t} dV = \iiint_V \rho \mathbf{f} dV - \oint_S p d\mathbf{S} \quad (15)$$

It is possible to make an analogy with the second Newton law, where the left-hand side (LHS) of the equation is the change of linear momentum of the system, and the right-hand side (RHS) stands for the contributions of surface forces (pressure) and body forces (\mathbf{f}). Note that the contribution of frictional forces has been neglected since the flow is inviscid. The energy equation in integral form is given in equation (16).

$$\begin{aligned} & \iiint_V \dot{q} \rho dV - \oint_S p \mathbf{V} \cdot d\mathbf{S} + \iiint_V \rho (\mathbf{f} \cdot \mathbf{V}) dV \\ &= \iiint_V \frac{\partial}{\partial t} \left[\rho \left(e + \frac{V^2}{2} \right) \right] dV + \oint_S \rho \left(e + \frac{V^2}{2} \right) \mathbf{V} \cdot d\mathbf{S} \end{aligned} \quad (16)$$

The first integral on the LHS stands for the rate of heat added to the fluid inside the control volume, while the second and third integrals stand for the rate of work done by the fluid. The RHS is the rate of change of energy of the fluid as it flows through the control volume. The variable e is the specific internal energy of the fluid. These equations can also be given in differential form.

The integral form of conservation equations captures overall quantities over a region, while derivatives provide point-wise information. This distinction influences their utility in modelling, analysis, and solving fluid flow problems. However, the meaning of the equations remains the same. Note that CFD makes use of the derivative formulation, which is solved by employing numerical methods such as the Finite Volume Method (FVM). Equations (17), (18) and (19) stand for the continuity, momentum and energy conservation equations in their derivative form, respectively.

$$\frac{\partial \rho}{\partial t} + \nabla \cdot (\rho \mathbf{V}) = 0 \quad (17)$$

$$\begin{aligned} \frac{\partial(\rho u)}{\partial t} + \nabla \cdot (\rho u \mathbf{V}) &= -\frac{\partial p}{\partial x} + \rho f_x \\ \frac{\partial(\rho v)}{\partial t} + \nabla \cdot (\rho v \mathbf{V}) &= -\frac{\partial p}{\partial y} + \rho f_y \\ \frac{\partial(\rho w)}{\partial t} + \nabla \cdot (\rho w \mathbf{V}) &= -\frac{\partial p}{\partial z} + \rho f_z \end{aligned} \quad (18)$$

$$\begin{aligned} \frac{\partial}{\partial t} \left[\rho \left(e + \frac{V^2}{2} \right) \right] + \nabla \cdot \left[\rho \left(e + \frac{V^2}{2} \right) \mathbf{V} \right] \\ = -\nabla \cdot (p \mathbf{V}) + \rho \dot{q} + \rho (\mathbf{f} \cdot \mathbf{V}) \end{aligned} \quad (19)$$

Equation (18) is a set of three equations, one for each component of the velocity vector, giving a total of five conservation equations. Nonetheless, a three-dimensional problem would consist of the following six unknowns u , v , w , p , ρ and e , and an extra equation is necessary to close the system. This additional equation is typically the EOS of the fluid, $p = \rho RT$ for an ideal gas, where R is the specific gas constant. If the flow was incompressible, the system would be undetermined and special methods would be needed to solve it.

D. One-Dimensional Normal Shock Wave Relations

This section discusses the one-dimensional normal shock-wave relations for static and moving shock waves, relative to the frame of reference. From the integral form of the conservation equations (14), (15) and (16) applied to a one-dimensional domain, it is possible to get the one-dimensional steady and inviscid relations of the flow. These are given in equations (20), (21) and (22) for mass, momentum and energy, respectively. The specific enthalpy is defined as $h = e + p/\rho$.

$$\rho_1 u_1 = \rho_2 u_2 \quad (20)$$

$$p_1 + \rho_1 u_1^2 = p_2 + \rho_2 u_2^2 \quad (21)$$

$$h_1 + \frac{u_1^2}{2} + q = h_2 + \frac{u_2^2}{2} \quad (22)$$

Now, it is crucial to define the speed of sound and Mach number. The speed of sound is given in equation (23).

$$a^2 = \left(\frac{\partial p}{\partial \rho} \right)_s \xrightarrow{\text{Perfect Gas}} a^2 = \frac{\gamma p}{\rho} = \gamma RT \quad (23)$$

The process inside the sound wave must be isentropic. Note that by perfect gas it is meant calorically perfect, where the specific heats of the gas are constant, and the energy and enthalpy are sole functions of the temperature. The Mach number is then defined as $M = \frac{V}{a}$.

1) *Normal Shock Waves in a Perfect Gas:* The conservation equations must be solved for the shock wave, where there is a sudden change of thermodynamic properties in an infinitely thin region, as illustrated in Figure 5. Note that the process is adiabatic ($q = 0$) but not isentropic, and therefore is irreversible. By introducing the Mach number into the one-dimensional flow equations, using the ideal gas law and doing algebraic modifications, it is possible to obtain the normal shock relations. These relations are expressed as a function of the incident Mach number $M_1 = \frac{u_1}{a_1}$, where u_1 is the incident speed of the fluid relative to the static normal shock, and a_1 the corresponding speed of sound.

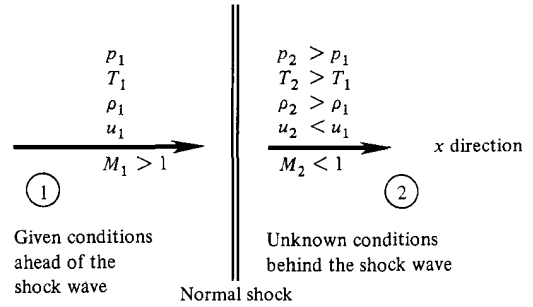


Fig. 5: Diagram of a static normal shock [20].

The relations for M_2 , $\frac{\rho_2}{\rho_1}$, $\frac{p_2}{p_1}$ and $\frac{T_2}{T_1}$ for a static normal shock wave in a perfect gas as a function of M_1 are given in equations (24), (25), (26), and (27), respectively.

$$M_2^2 = \frac{1 + [(\gamma - 1)/2] M_1^2}{\gamma M_1^2 - (\gamma - 1)/2} \quad (24)$$

$$\frac{\rho_2}{\rho_1} = \frac{u_1}{u_2} = \frac{(\gamma + 1) M_1^2}{2 + (\gamma - 1) M_1^2} \quad (25)$$

$$\frac{p_2}{p_1} = 1 + \frac{2\gamma}{\gamma + 1} (M_1^2 - 1) \quad (26)$$

$$\frac{T_2}{T_1} = \left(\frac{p_2}{p_1} \right) \left(\frac{\rho_1}{\rho_2} \right) = \left[1 + \frac{2\gamma}{\gamma + 1} (M_1^2 - 1) \right] \left[\frac{2 + (\gamma - 1) M_1^2}{(\gamma + 1) M_1^2} \right] \quad (27)$$

Regarding moving normal shock waves, the idea is completely analogous but putting the reference frame on an inertial external observer. Now $u_1 = W$ and $u_2 = W - u_p$, where W is the shock wave speed, and u_p is the speed of the gas behind the shock wave. Very similar algebraic modifications can be done to solve the one-dimensional conservation equations for W and u_p . The relations for W , u_p , $\frac{\rho_2}{\rho_1}$ and $\frac{T_2}{T_1}$ for a moving normal shock wave in a perfect gas as a function of $\frac{p_2}{p_1}$ are given in equations (28), (29), (30), and (31), respectively.

$$W = a_1 \sqrt{\frac{\gamma+1}{2\gamma} \left(\frac{p_2}{p_1} - 1 \right) + 1} \quad (28)$$

$$u_p = \frac{a_1}{\gamma} \left(\frac{p_2}{p_1} - 1 \right) \left(\frac{\frac{2\gamma}{\gamma+1}}{\frac{p_2}{p_1} + \frac{\gamma-1}{\gamma+1}} \right)^{1/2} \quad (29)$$

$$\frac{\rho_2}{\rho_1} = \frac{1 + \frac{\gamma+1}{\gamma-1} \frac{p_2}{p_1}}{\frac{\gamma+1}{\gamma-1} + \frac{p_2}{p_1}} \quad (30)$$

$$\frac{T_2}{T_1} = \frac{p_2}{p_1} \left(\frac{\frac{\gamma+1}{\gamma-1} + \frac{p_2}{p_1}}{1 + \frac{\gamma+1}{\gamma-1} \frac{p_2}{p_1}} \right) \quad (31)$$

2) *Normal Shock Waves in Water:* Several explosions carried out in this thesis are in water. Therefore, it is crucial to have relations between pressure and density over a normal shock wave in water. A typical EOS for water is the well-known modified Tait equation (32).

$$p - p_0 = B(S)[(\rho/\rho_0)^n - 1] \quad (32)$$

The parameter $B(S)$ is a function of the entropy only, which can be proved to be $B(S) = \rho_0 a_0^2 / n$ according to Sadi Ridah [21]. By using p and ρ data in the region of 20–60°C and 0–25 kbars, a value of $n = 7$ can be used. Employing $a_0 = 1500$ m/s for the sound speed of water in standard conditions, the parameter $B(S)$ becomes 3214 bar. Therefore, the modified Tait equation yields expression (33).

$$p - p_0 = 3214.0[(\rho/\rho_0)^7 - 1] \quad (33)$$

Now, by mixing equation (33) with the one-dimensional continuity (20) and momentum equations (21), it is possible to obtain equation (34) for normal shock wave in water, where $\zeta = \rho_2/\rho_1$ is a function of the incident Mach number M_1 .

$$(\zeta)^8 - (\zeta)(1 + 7M_1^2) + 7M_1^2 = 0 \quad (34)$$

Note that this equation has eight possible solutions, although most of them will be imaginary. The physical solution is the one giving real $\zeta > 1$. Once the density behind the shock wave is computed, the pressure can be obtained from the Tait equation. For a moving shock wave in water, the shock wave speed is coupled with the speed of the fluid behind the shock by means of the continuity equation. Rearranging it for u_p , it is possible to find the relation given in equation (35).

$$\rho_1 W = \rho_2(W - u_p) \longrightarrow u_p = W \left(1 - \frac{\rho_1}{\rho_2} \right) \quad (35)$$

E. Exploding Wire Magnetohydrodynamics

This section delves into the mechanism of the exploding wire and its connection with the flow parameters. Driving a very high current into a small conductive wire heats it up by

conductive processes. As the internal temperature of the wire increases, it changes phase from solid-to-liquid, from liquid-to-gas and from gas-to-plasma within hundreds of nanoseconds. When the wire vaporizes, the electrical conductivity of the material decreases rapidly, and thus the current also decreases abruptly. A very high voltage spike of tens of kV is induced to compensate for this sudden decrease in current. This instant is considered to initiate the explosion and is close to a maximum in the electrical power transferred to the wire.

When the wire is in the gas and plasma state, it is abruptly expanded changing its electrical properties. Part of the energy goes to expand the wire, and part of it goes to create a hotter ionized plasma. Equation (36) stands for the resistivity of the wire as a function of its radius, which changes in time.

$$R_w(t) = \frac{l}{\int_0^{R(t)} \sigma(R) \cdot 2\pi R(t) \cdot dR} \quad (36)$$

Note that σ denotes the conductivity of the material, typically copper, and l its length. Another relevant electrical parameter of the wire to determine the behaviour of the system is its self-inductance, which is given in equation (37).

$$L_w(t) = \frac{\mu_0 l}{2\pi} \left[\ln \left(\frac{2l}{R(t)} \right) - \frac{3}{4} \right] \quad (37)$$

This inductance is again a function of the geometrical properties of the wire. Note that μ_0 is the magnetic permeability in vacuum. Now, it is crucial to understand that as current flows through the wire, a voltage drop and electric field along the axis of the plasma channel are created. An expression to compute this electric field is given in equation (38).

$$E_z = \frac{i(t)R_w(t)}{l} \quad (38)$$

At the same time, an azimuthal magnetic flux will also appear as a consequence of Ampere's law. This electromagnetic field carries energy which modifies the thermodynamic state of the fluid. Kyoung-Jae Chung et al. [16] discuss this expansion process, giving a simple one-dimensional MHD model linking the fluid derivative conservation equations with the generated electromagnetic field. The model consists of the momentum equation, the equation of motion of the fluid, the energy conservation equation and Ampere's law as given in equations (39), (40), (41) and (42), respectively. Note that κ_c is the thermal conductivity, and Q_R is the volumetric radiation loss.

$$\rho \frac{du}{dt} = -\frac{\partial p}{\partial r} - \sigma E_z B_\theta \quad (\text{Momentum conservation}), \quad (39)$$

$$\frac{dr}{dt} = u \quad (\text{Equation of motion}), \quad (40)$$

$$\left(\frac{\partial e}{\partial T} \right)_\rho \frac{dT}{dt} + \left[p + \left(\frac{\partial e}{\partial \rho^{-1}} \right)_T \right] \frac{\partial \rho^{-1}}{\partial t} \quad (41)$$

$$= \rho^{-1} \left[\sigma E_z^2 + \frac{1}{r} \frac{\partial}{\partial r} \left(r \kappa_c \frac{\partial T}{\partial r} \right) - Q_R \right] \quad (\text{Energy conservation}),$$

$$\frac{1}{r} \frac{\partial}{\partial r} (r B_\theta) = \mu_0 \sigma E_z \quad (\text{Ampere's law}). \quad (42)$$

This system of equations formulated in cylindrical geometry couples the behaviours of the wire and surrounding medium, which need to be solved together with the ODE of the electrical system and the EOS of the materials. Solving it is challenging in terms of modelling the radiation losses, the heat conduction, the internal energy of the plasma and the electrical conductivity of copper. In the context of this thesis, this MHD system will not be solved, although it is crucial to understand how it differs from a simple hydrodynamic system. Note that the electromagnetic field has a relevant impact on the momentum and energy exchange.

When the current starts flowing through the wire, an external magnetic pressure field is created, making it more difficult for the wire to start expanding. Just after the wire explosion, after the voltage peak induced by the sudden decrease in electrical conductivity when the wire vaporizes, the wire starts expanding and ionizing rapidly, which creates a very fast shock wave in the surrounding medium. The resistivity of the wire drops, increasing again the current through the plasma channel. This process is called the current restrike, and has a relevant impact on the generated shock wave since the magnetic pressure will be feeding it from the upstream direction. Furthermore, the accelerating expanding wire behaves like a piston, compressing the adjacent medium until a peak in pressure is obtained. Compression waves are separated from the wire, propagating radially into the medium and feeding the shock. This process is especially important during the first instants after the shock wave is created, which adds up with the MHD effects to create a highly transient and non-linear process.

IV. METHODS

This section summarizes the methodology used in this study. The main focus points are the PPG, the system connections and the optical setup. A brief description of the employed hardware is included in the explanation of the system connections.

A. Pulsed Power Generator

A very thin wire is exploded using a PPG, which rapidly discharges currents in the order of hundreds of kA at voltages

in the order of tens of kV. Safety and reliability are a foremost topic in applications of high-voltage engineering, for which the margin of safety of the experimental setup must be very conservative both to protect life and hardware. The laboratory in which the experiments are conducted is divided into two areas: the control room and the test room. While experiments are conducted, researchers are located in the control room, the PPG is stationary and located in the test room. These two areas must be as isolated as possible. The PPG is a vertical machine consisting of three levels. The bottom level contains four big capacitors in parallel with a total capacitance of $C = 10 \mu\text{F}$, which can be charged up to 27 kV. The medium level contains the electrical circuit, consisting mainly of electrodes and spark gaps. The top level contains the test chamber where the wire is located vertically. A simplified sketch of the main electrical circuit is included in Figure 6.

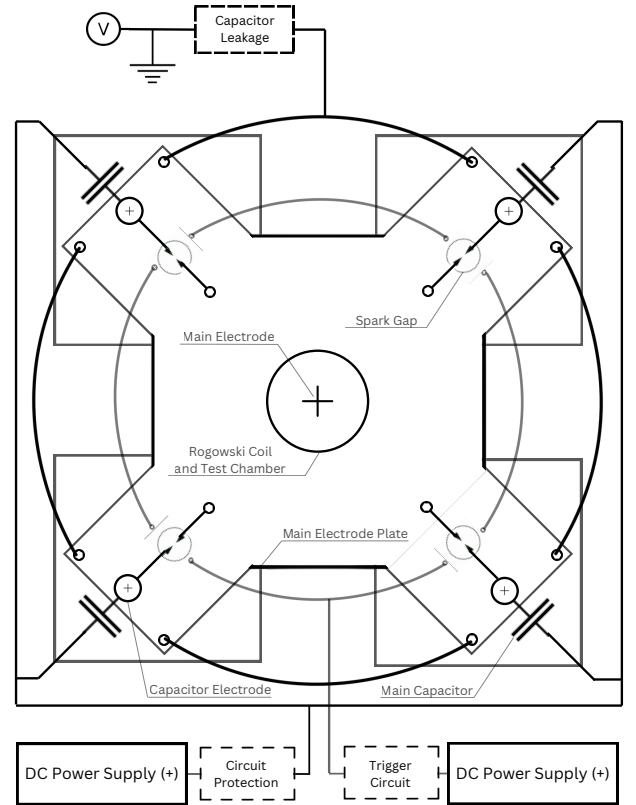


Fig. 6: Simplified sketch of the PPG.

The electrical circuit starts from two power supplies located in the test room. One of these charges the main capacitors of the PPG, and the other one charges the capacitors of the trigger circuit. Note that there is a secondary circuit for circuit protection between the supply and the capacitors. For this thesis, the main capacitors are charged up to a range between 19 – 24 kV. The four main capacitors have an electrode each, connected through spark gaps to the main electrode plate. These spark gaps only discharge current when the trigger circuit is remotely activated from the control room. The trigger circuit also discharges through spark gaps, which need to be flushed with dry air for correct operation. All the capacitors

are connected between them to ideally keep the same voltage level, and all the spark gaps are also connected to generate a simultaneous and precise discharge. As the current flows through the main electrode plate, all the energy is concentrated in the centre of the plate, where the main electrode is connected to the wire in the test chamber. Using a plate is a good configuration to minimize the total resistance and inductance of the system.

An RC is placed between the main electrode and the test chamber to instantaneously measure the total current flowing in the system. This element makes use of magnetic induction to measure current, which is proportional to the voltage outputted by the coil by means of the proportionality factor β_{RC} [A/V]. For more details regarding the operation of the RC, the reader is referred to David A. Ward and J. La T. Exon [22]. Finding the parameter β_{RC} is one of the tasks carried out in this thesis, referred to as calibration of the RC. The capacitors are all connected to a leakage circuit leading to the ground. This allows for constant discharge of the main capacitors as a safety measure. During experimental operation, the rate at which the capacitors are charged is greater than the rate at which the capacitors discharge to reach the desired voltages for explosions. Out of the leakage circuit, a BNC cable is connected to a digital voltmeter in the control room.

The whole setup is installed inside a thick grounded Faraday box. The test chamber is installed on top of this box vertically over the main electrode and RC. A picture of it is included in Figure 7. Note that the chamber has two windows installed to visualize the explosion thanks to an external light source coming from a laser. The window holders are made out of steel to hold the extreme conditions generated inside the test chamber. The system has two high-voltage probes installed: one connected to the main electrode plate, and the other to the bottom end of the wire. These are expected to measure different voltages mainly due to the inductance associated with the main electrode. The whole electrical system behaves very similarly to an RLC equivalent circuit with time-dependant resistance (see Section V-A).



Fig. 7: Picture of the RC and test chamber.

B. System Connections

This section details the various hardware components comprising the system and their interconnections. A simplified block diagram encompassing the different parts of the system is included in Figure 8.

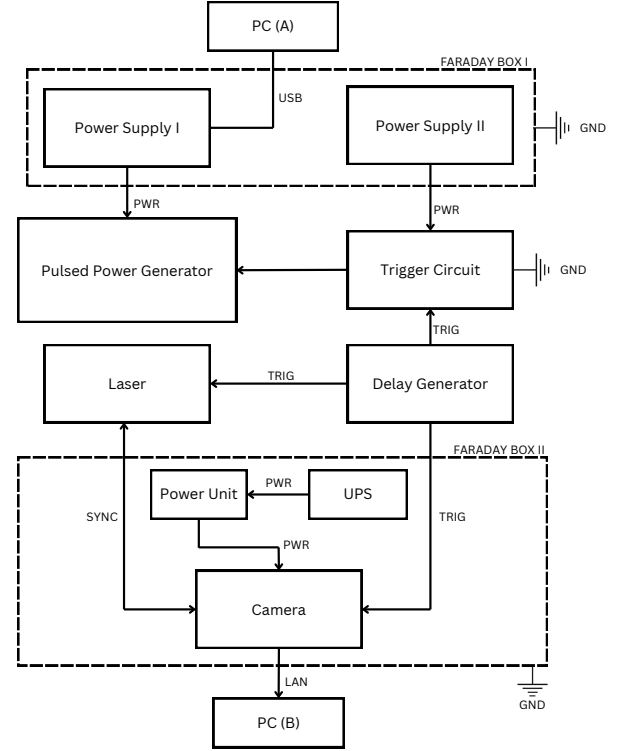


Fig. 8: Block diagram of the system connections.

The system contains two computers and two power supplies. The computer PC (A) is connected via USB to the Power Supply I connected to the capacitors, which is controlled from the control room. This power supply is a FUG MPL 500-50000 and can deliver up to 500 W of power at a maximum voltage of 50 kV. It is located in the Faraday Box I alongside the Power Supply II, which provides power to the trigger circuit and needs to be turned on manually before charging the capacitors. The second power supply is a SPELLMAN SL300 which can deliver up to 300 W of power at a maximum voltage of 10 kV. All the Faraday boxes are grounded since they are located in the test room. The second computer PC (B) is connected to a high-speed video camera via LAN cable with attenuation for over-voltage protection. This computer controls the operation of the camera via software.

The high-speed video camera is an HPV-X2, which can record 256 consecutive frames at a maximum rate of 10 million frames per second. The recording rate used in this thesis has been 5 million frames per second (or a frame every 200 nanoseconds). The high-speed frames have a resolution of 400 pixels (horizontal) x 250 pixels (vertical). It also has a live mode that is useful for aligning the optical equipment. The camera is synchronized with a laser controller via BNC

cable, which sends pulses at the same frequency at which the camera opens its sensor. The laser is a class 4 CAVILUX SMART 500 W pulsed laser with a wavelength of 690 ± 10 nm. Precise synchronization between the camera and the laser is crucial for obtaining good-quality images, as well as an adequate pulse duration for the laser. The camera is powered by an independent power unit fed by a Uninterruptible Power Supply (UPS). The UPS is connected to the building power supply via a power line filter, although it can also operate on battery mode for approximately ten minutes.

A delay generator is placed in the control room to manually send the trigger signals to the trigger circuit, the laser and the camera. These signals are sent simultaneously, and therefore the camera will start recording a few instants before the explosion begins (approximately $8 \mu\text{s}$). This time shift can be controlled by changing the signal delay time of the delay generator. The trigger is only sent once the capacitors are fully charged and the trigger circuit is ready for explosion. During the explosion, a video of the moving shock wave is recorded through the windows of the test chamber using the methods described in Section IV-C.

The voltage waveforms are measured at the main electrode plate and the bottom of the wire through two high-voltage probes. The probe measuring the voltage at the bottom of the wire is a Single-Ended TEKTRONIX P6015A, which can measure peaks up to 40 kV. This probe sends the attenuated measured voltage to a TEKTRONIX TDS 2014C oscilloscope placed in the test room. The probe measuring the voltage of the main electrode plate is handcrafted and it sends its signal to another oscilloscope of the same kind placed in the control room, which also records the corresponding current signal from the RC attenuated by 30 dB. Being able to replicate the voltage measured at the bottom of the wire utilizing the measurements of the voltage of the main electrode plate is one of the tasks carried out in this thesis. This is important to be able to characterize the voltages along the system by just using one high-voltage probe. Note that this configuration is actively evolving over time to meet the requirements of the experiments, although it has remained mainly unchanged for the explosions conducted in this thesis.

C. Optical Setup

This section summarizes the optical setup employed to visualize the experiments. The main idea behind the setup has been explained in Section III-B. A z-type-based mirror system is used, either in Shadograph configuration for water explosions or in Schlieren for air explosions. This distinction is necessary since the air explosions saturate the camera images with too much light, so a knife-edge needs to be used to cut off the refracted light. A sketch is included in Figure 4. In the laboratory setup, The light source is the CAVILUX SMART laser instead of a lamp, so the light already comes from a point source and there is no need to include a slit.

The laser controller, which is located in the control room, is connected via an optical fibre cable to a laser diode placed

in the test room. The laser diode outputs divergent light, which is collimated using a first parabolic mirror and sent to a plane mirror before the test region. This plane mirror redirects the light through the windows of the test chamber where the experiment is conducted. The light arrives then at a second parabolic mirror that converges it. For reasons of space arrangement in the test room, the converging light is redirected via a second plane mirror before it focuses. If air explosions are carried out, a knife-edge is placed at this light focus to get Schlieren images. After the focus, the light diverges again until it gets to the Faraday box where the camera is placed, which contains a hole with a wavelength filter at 690 nm. A picture illustrating the optical arrangement after the second parabolic mirror is given in Figure 9.

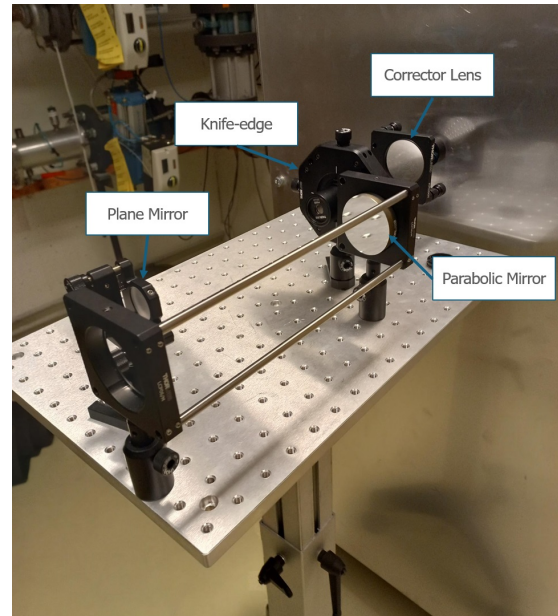
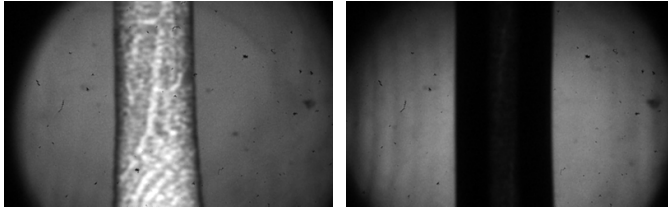


Fig. 9: Optical arrangement in front of the camera box.

Figure 9 shows an important deviation from the explained setup: a corrector lens between the knife edge and the wavelength filter. A Schlieren image using a knife edge loses focusing quality since the focal length of the second parabolic mirror is much shorter than the length of the test region. In Sivana M. Torres et al. [23], the authors investigate this focusing challenge in Schlieren imaging systems with extended test sections (where the parallel light test section is longer than the focal length of the focusing Schlieren optics). Due to limitations in the focusing optics, only a specific region within the test section can be clearly imaged. The study explores the use of corrector lenses to manipulate the focal zone within the test section. They test various corrector lens strengths (long to short focal lengths) in both lens-based and mirror-based Schlieren systems. Additionally, they examine how different collecting optic focal lengths affect focus. They conclude that it is possible and crucial to use corrective lenses in Schlieren systems to improve image focusing.

In the experimental setup, a bi-convex positive lens with a focal length of 100 mm is used to improve the Schlieren images. This gives a significant improvement, although it still

does not focus the test region perfectly. On the other hand, Shadowgraph images appear more focused since they are mere shadows. Figure 10 is included to compare the differences between two explosions recorded in air and water with Schlieren and Shadowgraph, respectively. From the images, it can be seen that Schlieren is less focused, although it gives more level of detail. The images show a shock wave expanding radially, the physical process is explained in the results Section V-B1.



(a) Schlieren in air.

(b) Shadowgraph in water.

Fig. 10: Example images of Schlieren and Shadowgraph for explosions of $\varnothing 150\ \mu\text{m}$ wires at $v_C(0) = 23\ \text{kV}$.

D. Explosion Procedure and Safety Considerations

This section summarizes in a list the experimental procedure necessary for a safe explosion. Only authorized researchers with a full understanding of this procedure are allowed to be in the laboratory during an explosion.

- (i) Make sure that all the necessary hardware is in its place, and the power breakers of the PPG, trigger circuit and power supplies are off. After checking, a wire can be soldered and installed inside the test chamber. Put water inside the chamber if intended.
- (ii) Turn on the power breakers of the PPG, trigger circuit and power supplies. Open the valve for dry air used to prepare spark gaps for the explosion. Flush the spark gaps with dry air.
- (iii) Connect the TEKTRONIX high-voltage probe to the oscilloscope in the test room. The second high-voltage probe and the RC are sent to an oscilloscope placed in the control room. Make sure that the oscilloscopes are waiting for the trigger signal on a single sequence.
- (iv) Open the camera box and turn on the UPS and the camera. Close the camera box. Make sure that the box is connected to LAN cable, power cable and ground.
- (v) Turn on the computers and the laser. Turn on the safety blinking light outside the room indicating ongoing laser operation. The optical setup can be aligned by using the live mode of the camera and the laser connected to a function generator. Wear protective glasses and install the knife-edge if necessary. Once the optical arrangement is correct, turn off the laser, connect it to the trigger and synchronization cables, and turn on the laser again without triggering it.
- (vi) Turn on the delay generator and perform a first recording test triggering the camera and laser manually. Make sure

that there is a good video at the desired rate of frames per second. Modify the pulse duration of the laser to get the desired brightness on the image.

- (vii) Turn on the power supplies. Make sure that there is a connection between FUG and the computer PC (A) using the FUG software. If not, check the USB cable used for the communication.
- (viii) Go to the control room and check that everything is in its place. Double-check that the camera box is closed. Flush the spark gaps with dry air and turn on the switch of the trigger circuit.
- (ix) Activate the SPELLMAN power supply which charges the trigger circuit. For safety reasons, leave the test room immediately and close the two doors between the test and control rooms. Perform a second recording test triggering the system manually from the delay generator, expect now to hear the discharge of the trigger circuit.
- (x) Two people are necessary for the experiment. One person will be sitting at PC (A) controlling the charging level of the capacitors. The other person will be sitting at PC (B) preparing the camera and laser for the trigger. Everyone in the room needs to wear earmuffs. The person on PC (A) starts charging the capacitors by using the FUG software.
- (xi) While the capacitors are charging, the person on PC (B) makes sure that the camera and laser are ready. When the capacitors are charged at the desired voltage level (never more than 26 kV for the PPG design conditions), the person at PC (A) immediately turns off the charging of the capacitors and triggers the delay generator manually. This will now provoke the explosion.
- (xii) After the explosion, wait between 10-20 seconds. The person on PC (B) turns off the laser. The person on PC (A) enters the test room to turn off the SPELLMAN power supply manually. It is crucial to avoid any type of physical contact with the PPG or trigger circuit. Go back to the control room and wait 20 minutes until the capacitors are fully discharged. Turn off the safety blinking light outside the room indicating ongoing laser operation.
- (xiii) Once the capacitors are discharged, it is allowed to enter the test room again. Make sure to save the data from the oscilloscopes on an external USB. Turn off the power supplies, oscilloscopes, delay generator and the switch of the trigger circuit. Turn off the power breakers of the PPG, trigger circuit and power supplies. Close the valve of the dry air, and open the camera box to turn off the camera and the UPS. Open and clean the test chamber. Turn off the computers.

There are identified only three possible sources of fatal error. The first fatal error consists of a failure of the trigger circuit, not triggering the explosion. If this happens, let the capacitors discharge completely and then turn off the SPELLMAN power supply. The second fatal error consists of an uncontrolled discharge of the capacitors while the FUG power supply is still

trying to charge them. In this case, turn off the FUG remotely and let the capacitors discharge completely. The third fatal error consists of a failure of the FUG software, not stopping the charging of the main capacitors. If this happens, press the emergency button cutting off the power supply of the laboratory. Do not hesitate to press the emergency button in case of physical hazard.

V. RESULTS

This section provides the results regarding the electrical characterization of the PPG, the shock wave generation and the electrical-to-mechanical energy conversion. In terms of experiments, the electrical characterization encompasses only short-circuit discharges, while the rest of the work encompasses several single-wire explosions.

A. Electrical Characterization of the PPG

The goal of this section is to provide a validated electrical model to analytically and numerically replicate the behaviour of the PPG in short-circuit experiments. By doing this, an electrical framework of the functioning of the PPG during wire explosions is also determined, since the only varying parts of the electrical system are the electrical loads in the test chamber.

1) *Short Circuit Experimental Results:* The short circuit experiments are carried out in air utilizing a thick threaded rod in the test chamber instead of a thin wire. By doing this, there is no explosion in the test chamber, and the main electrode is connected to the ground through the rod closing the system, which behaves like an equivalent RLC. A picture of a short circuit experiment during discharge is included in Figure 11, which shows a vertical rod and a diagonal cable (used to measure voltage waveforms using the TEKTRONIX high-voltage probe). It is interesting to see that weak shock waves are generated from the bottom and top supports of the rod due to dielectric discharge in the proximities between the rod and its supports. This image is taken using Shadowgraph, since these experiments do not light-saturate the images. Reflections of these weak shock waves can be observed at the serrated edges of the threaded rod.

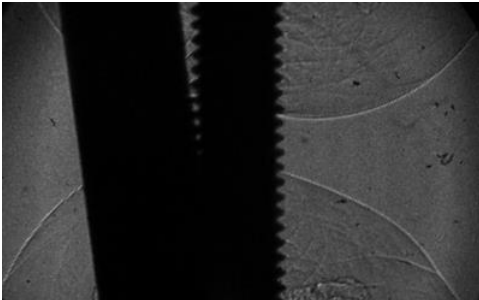


Fig. 11: Picture of a non-explosive short circuit discharge through a threaded rod.

The results of these short circuit experiments for initial capacitor voltages of $v_C(0) = 19$ kV and $v_C(0) = 24$ kV are included in Figure 12. Note that v_1 describes the voltage measured at the main electrode plate, and v_2 corresponds to the voltage at the bottom of the threaded rod. These voltages include both inductive and resistive contributions for now. As expected from these experiments, $v_2 < v_1$ at all times, since the equivalent inductance and resistance of the circuit between the two probes are storing and consuming energy. The TDT of both experiments is around $30 \mu\text{s}$, although it is slightly higher for $v_C(0) = 24$ kV since there is more energy within the system to be dissipated. For the sake of comparison, the total energy available in the system is given by $E_a = \frac{1}{2} C v_C(0)^2$, which yields 1805 J for $v_C(0) = 19$ kV and 2880 J for $v_C(0) = 24$ kV (or 59% more energy for the second case). Note that the voltage is smaller than $v_C(0)$ at all times, and the current almost gets to 300 kA for the most extreme case. How β_{RC} is determined to get the current measurement is explained in the following Section V-A2.

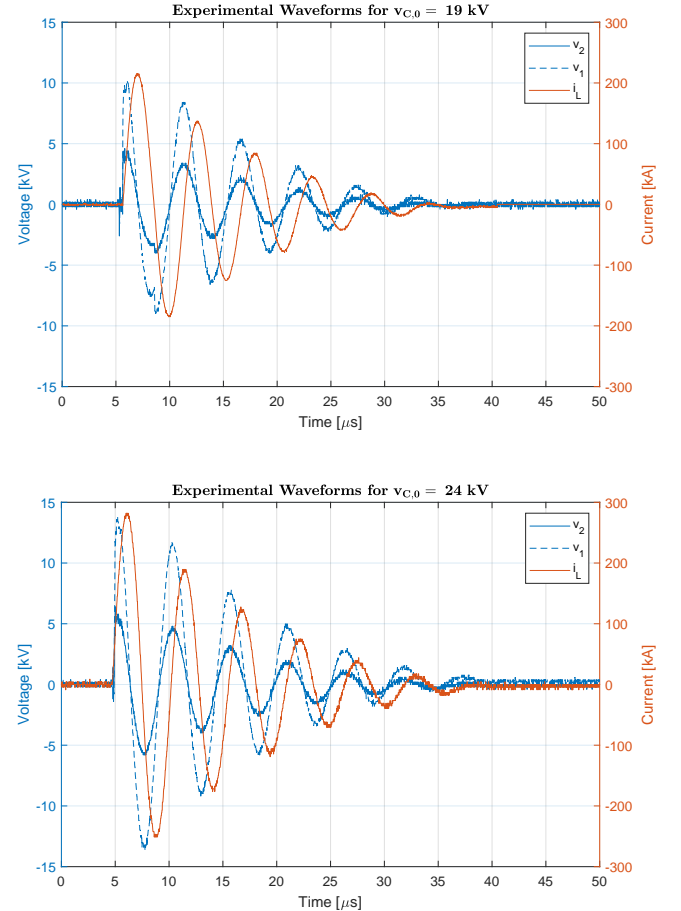


Fig. 12: Experimental short circuit waveforms for different initial capacitor voltages.

2) *Analytical Model Analogy:* To replicate the experimental waveforms of Figure 12, the system is modelled with an RLC-like second-order circuit with variable resistivity. The variable resistivity is necessary since the behaviour of the spark gaps is not linear and introduces non-constant energy dissipation.

Furthermore, the resistivity created by the generated plasma channel in the spark gaps is non-negligible, and it makes a major contribution to the resistivity of the system. Similarly to Kyoung-Jae Chung et al. [16], the system is modelled in parts utilizing the electrical circuit given in Figure 13.

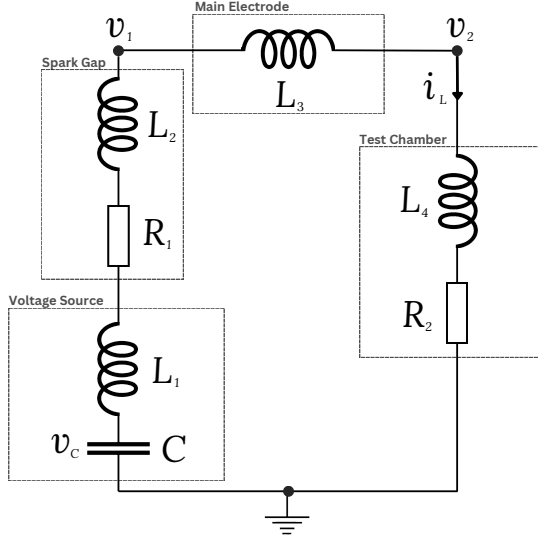


Fig. 13: Analogy of the PPG Electrical Circuit.

The voltage source encompasses the main capacitors of the system, which are given a total capacitance C and inductance L_1 . The spark gaps are given a variable resistance R_1 and total inductance L_2 . The main electrode is only given an inductance L_3 , since experimental measurements of its resistivity give negligible resistances in the order of $\mu\Omega$. The loads of the test chamber are associated with the inductance L_4 and resistivity R_2 of the threaded rod. This last part is different when approaching wire experiments, but the rest of the system remains constant. Experimentally, it has been found that R_2 is also in the order of $\mu\Omega$ for the short circuit experiments, but it is included in the diagram for the sake of generalization since a very thin wire would have significant resistance.

In order to determine the value of these electrical loads, we try to match the experimental waveforms with the analytical waveforms equations for $v_C(t)$ and $i_L(t)$ given in equations (11) and (12), respectively. The analysis starts by computing equivalent RLC parameters assuming that the main source of resistivity in the system is given by R_1 , which is not constant. At the very beginning of the discharge, the plasma channel of the spark gap offers relatively small resistance to the current. As time evolves, this plasma channel diffuses in the surrounding medium, decreasing the density of the plasma and making it harder for the current to flow. Therefore, this resistivity increases in time, which in turn increases the damping ratio of the system $\alpha = \frac{R}{2L}$. For a first RLC approach with constant coefficients, the average damping ratio of the system will be used. It is known from Agarwal [18] that the envelope of the electrical waveforms in a second-order RLC system simply follows an exponential decay with $e^{-\alpha t}$. By fitting this envelope in the voltage waveforms of Figure 12, it is possible to find an

average damping ratio of $\alpha = 90\,600\,\Omega/\text{H}$. Furthermore, it is known that the damped frequency of the system $\omega_d = \frac{2\pi}{T_d}$ can be computed from the damped period, which has an average value of $T_d = 5.5072\,\mu\text{s}$ from the experimental waveforms, yielding an average $\omega_d = 1.1409 \cdot 10^6\,\text{rad/s}$. Now the natural frequency of the system can be computed as $\omega_0 = \sqrt{\omega_d^2 + \alpha^2}$. Since $\omega_0 \geq \omega_d$ and $\alpha \ll \omega_d$, the system is highly under-damped with natural and damped frequencies similar in value. Thus, the natural frequency of the system in kilohertz yields $f_0 = 181\,\text{kHz}$.

The equivalent average resistivity R and inductance L of the system can be found using $\alpha = \frac{R}{2L}$, $\omega_0 = \frac{1}{\sqrt{LC}}$ and knowing $C = 10\,\mu\text{F}$, yielding $R = 13.3\,\text{m}\Omega$ and $L = 73.279\,\text{nH}$. At this point of the analysis, the total capacitance and inductance of the system will be considered constant, but the resistivity will be changed manually around the value R to fit an empirical relation $R(k, t)$ that matches the analytical waveforms of equations (11) and (12) with the experimental results. Note that k is a function of the initial capacitor voltage. The experimental inductive voltage needs to be added to the resistive voltage of the system to compute the transient voltage $v_C(t)$ in the capacitors. This is done by solving $v_C(t) = R(k, t) \cdot i_L(t) + L \cdot \frac{di_L}{dt}$ with the experimental results, the constant total inductance and the time-changing empirical resistance. The experimental waveforms are matched with the analytical solution in an iterative process where β_{RC} is determined. The empirical relation for the resistivity $R(k, t)$ that matches the results is given in equation (43), where $T = 5 \cdot 10^{-5}\,\text{sec}$ and $R_0 = 0.0133\,\Omega$, and the voltage of the empirical parameter k needs to be inputted in kV. The parameter β_{RC} is fully determined and given in (44).

$$R(k, t) = 0.2kR_0 + k \frac{1.8R_0}{T^{0.84k}} t^{0.84k}, \text{ with } k = \frac{19}{2 \cdot v_C(0) - 19}. \quad (43)$$

$$\beta_{RC} = 696.59 \frac{\text{A}}{\text{V}}. \quad (44)$$

This resistance matches extraordinarily well the system's behaviour, as shown in Section V-A4, and its non-linear behaviour is associated with the time-increasing resistance of the plasma channel in the spark gaps defined as R_1 . It is also determined that there is an attenuation equivalent to 30 dB between the test and control rooms in the current signal. For the measurement of v_1 , it is determined that there is a voltage proportionality factor of 2.5 kV/V between the signal received in the control room and the voltage measured by the high-voltage probe. For the measurement of v_2 with the TEKTRONIX probe in the test room, this proportionality factor is 1 kV/V. The parameters L_1 , L_2 , L_3 and L_4 are now computed, knowing $L_1 = 10\,\text{nH}$ for the design condition of the capacitors, and solving the system of three equations and three unknowns given in equations (45), (46) and (47). The resistance R_2 has been simplified to $R_2 \approx 0\,\Omega$ for this application since it is three orders of magnitude smaller than R_1 .

$$v_2 = L_4 \cdot \frac{di_L}{dt} \quad (45)$$

$$v_1 = (L_4 + L_3) \cdot \frac{di_L}{dt} \quad (46)$$

$$L = L_1 + L_2 + L_3 + L_4 \quad (47)$$

A summary of the results from this analysis is given in Table I. Remember that the resistance of the spark gap is given by the empirical equation (43), which is a function of the initial voltage in the capacitors and increases in time. The parameters of the test chamber are only valid for the given threaded rod and will be different during wire explosion.

TABLE I: Summary of the electrical parameters of the PPG.

Electrical Parameters	Voltage Source	Spark Gap	Main Electrode	Test Chamber
Inductance [nH]	10	22.5	23.3	17.5
Resistance [mΩ]	-	2.7 - 26.6	-	≈ 0
Capacitance [μF]	10	-	-	-

3) *Numerical Model Simulation:* A third approach involving a numerical simulation is used to further validate the results obtained from matching the experimental waveforms with the analytical solution of an RLC system. This numerical solution is performed using the commercial software LTspice from Analog Devices [24], which uses the popular solver SPICE for analog circuits. The SPICE simulator employs a mathematical approach, using Kirchhoff's loop laws to establish a system of differential equations. By solving these equations, the simulator can predict circuit behaviour with high accuracy and speed. To achieve this, SPICE assigns nodes to the circuit and calculates the current and voltage at each one. This process involves generating the equations in a matrix format, which SPICE then solves to find the unknown values. The number of iterations required to solve the equations can vary depending on the complexity of the circuit. A circuit analogous to the one defined in Figure 13 is designed in LTspice, yielding the circuit of Figure 14. The values of Table I are used to run a transient simulation. The obtained results are given and compared in the following Section V-A4.

4) *Comparison of the Models:* This section compares the voltage and current waveforms obtained experimentally, analytically and numerically. The comparison of the short circuit discharges for initial capacitor voltages of 19 kV and 24 kV is illustrated in Figure 15. For each initial capacitor voltage, the corresponding plot contains three waveforms for the voltage and three waveforms for the current, which relate to the waveforms obtained experimentally, analytically and numerically. There is an excellent agreement between the experimental data and the analytical results. The numerical simulation differs slightly more from the experimental results, particularly for later stages. Both models have a correlation factor with the experimental results greater than $R^2 \geq 0.95$ in all cases. These results could be improved by finding a more accurate expression for the resistance of the spark gap to match better the actual damping ratio of the system. Nonetheless, the

high correlation between the two models with the experimental results validates the electrical parameters of the PPG given in Table I, as well as all the assumptions made for their calculation.

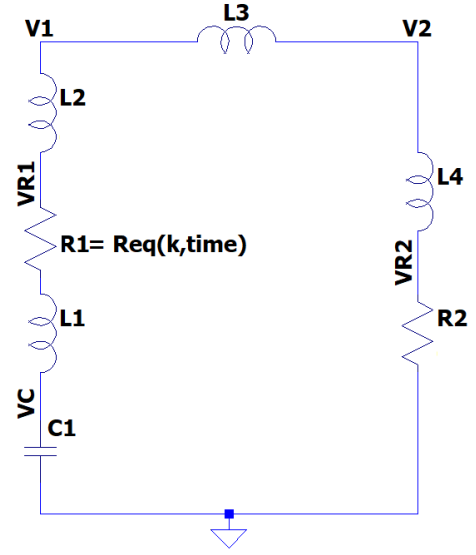


Fig. 14: Circuit designed and simulated in LTspice.

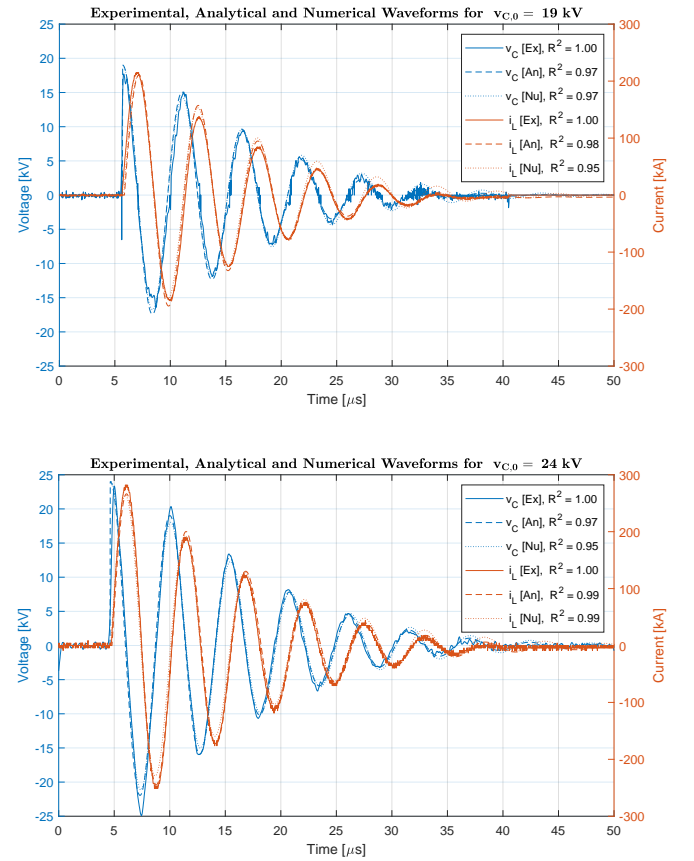


Fig. 15: Comparison of the experimental, analytical and numerical short circuit waveforms.

B. Shock Wave Generation

Several explosions are carried out in air and water for different wire diameters and initial capacitor voltages. More concretely, three different wire sizes of $\varnothing 150 \mu\text{m}$, $\varnothing 400 \mu\text{m}$ and $\varnothing 500 \mu\text{m}$ are exploded at initial capacitor voltages of 19 kV, 21 kV and 23 kV in air. The same is done in water but only for an initial capacitor voltage of 23 kV. This yields a total number of 12 explosions, 9 in air and 3 in water.

This section summarizes all the results obtained from the shock wave generation through these single-wire explosions. It contains a characterization of the shock wave by means of studying the camera recordings, an analysis of the electrical waveforms during the explosions, a study of how the electrical energy is transferred from the PPG to the wire, a model to estimate the mechanical energy transferred to the shock wave by the wire expansion, and an analysis of the electrical-to-mechanical energy transfer efficiency.

1) *Video Analysis of the Shock Wave Position:* The shock wave is characterized thanks to the HPV-X2 video recordings of the explosions. A frame-by-frame analysis of these recordings can be done to find the position of the shock wave with respect to time. Figure 16 is included to exemplify one of these recordings, showing several handpicked frames of a $\varnothing 400 \mu\text{m}$ wire explosion and $v_C(0) = 23 \text{ kV}$ in water using Shadowgraph. The first frame (a) corresponds to instants before the explosion, with a wire installed vertically in the test chamber filled with water. In less than a microsecond, the PPG is triggered discharging a huge current through the wire and making it explode. The second frame (b) is taken a few instants after the explosion, showing a very bright and hot copper plasma expanding in the centre of the image. The shock wave is already generated and detached from the CS between the wire and the surrounding water.

The third frame (c) shows the shock wave moving in a radial direction faster than the CS, where the shock front is clearly delimited by a sudden change in light intensity expanding radially. The fourth (d), fifth (e) and sixth (f) frames show the continuous radial expansion of both the shock wave and CS. Note that a second shock is formed from the top and bottom of the image, corresponding to the explosion of the solder holding the wire. The shock front is almost outside the image in a time of $7.6 \mu\text{s}$, although this process happens much faster in air. Since the image contains 400 pixels in the horizontal direction and the pixel-per-millimetre ratio is approximately 10 pixels/mm, the shock front travels a radial distance smaller than 20 mm in this time span. One can already observe that the shock front speed is in the order of km/s.

The speed of the generated shock waves can be found by systematically analysing these recordings and taking the derivative of the position of the shock wave front. Once this speed W is known, the corresponding Mach number of the travelling shock is computed as $M_1 = \frac{W}{a_1}$, where a_1 is approximately 343 m/s for air and 1,481 m/s for water. Once the Mach number of the shock front is computed, the shock wave jump relations (28) and (29) are used for air

to compute the pressure and the speed of flow behind the shock, respectively. For water, relations (33), (34) and (35) are used instead. Since the speed of the shock front is expected to decrease in time as the shock wave expands radially, the pressure and speed behind the shock are expected to decrease too. An example of this is given in Figure 17, where the evolution of the SW is illustrated for air and water explosions with $\varnothing 500 \mu\text{m}$ and $v_C(0) = 23 \text{ kV}$.

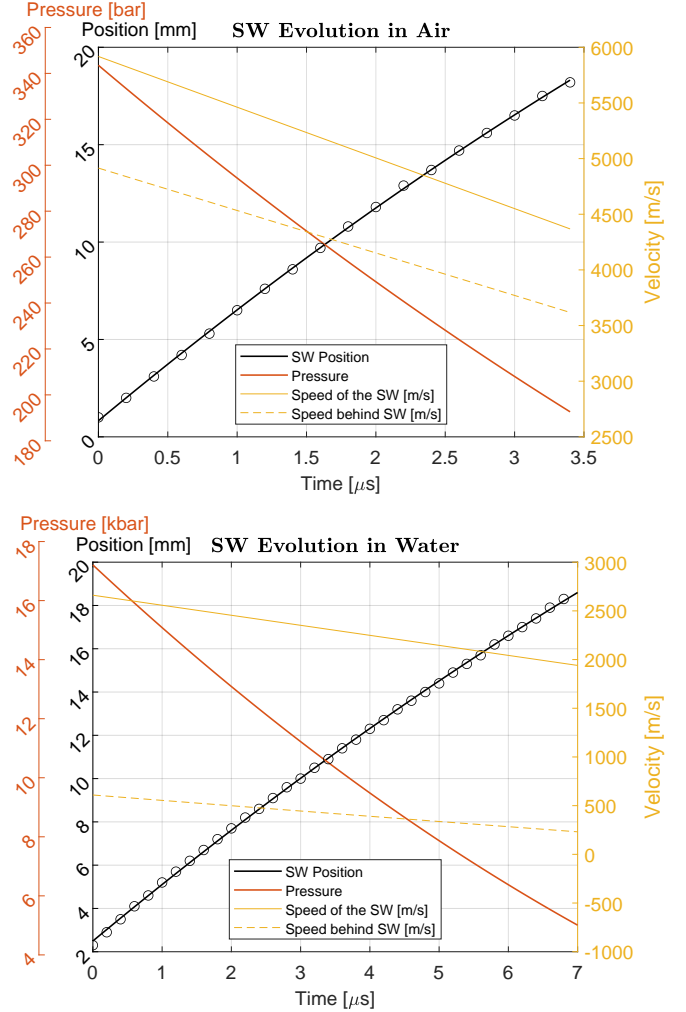


Fig. 17: Evolution of the shock wave position, shock wave speed, speed of the gases and pressure behind the shock wave for air and water explosions with $\varnothing 500 \mu\text{m}$ and $v_C(0) = 23 \text{ kV}$.

It can be observed that the shock wave generated in the air moves approximately twice as fast as in water. This translates into having approximately twice as many experimental data points from the camera recordings in water. The speed behind the gases is strongly supersonic in air explosions, while it is subsonic for water. Despite having a much slower shock wave, the pressure behind the shock achieved in water is significantly higher than in air, approximately 60 times greater in water being in the order of tens of kbar (or GPa). During the studied time scale, the position of the shock wave can be greatly fitted with a second-order polynomial, thus having a linearly decreasing speed. This leads to the conclusion that the first

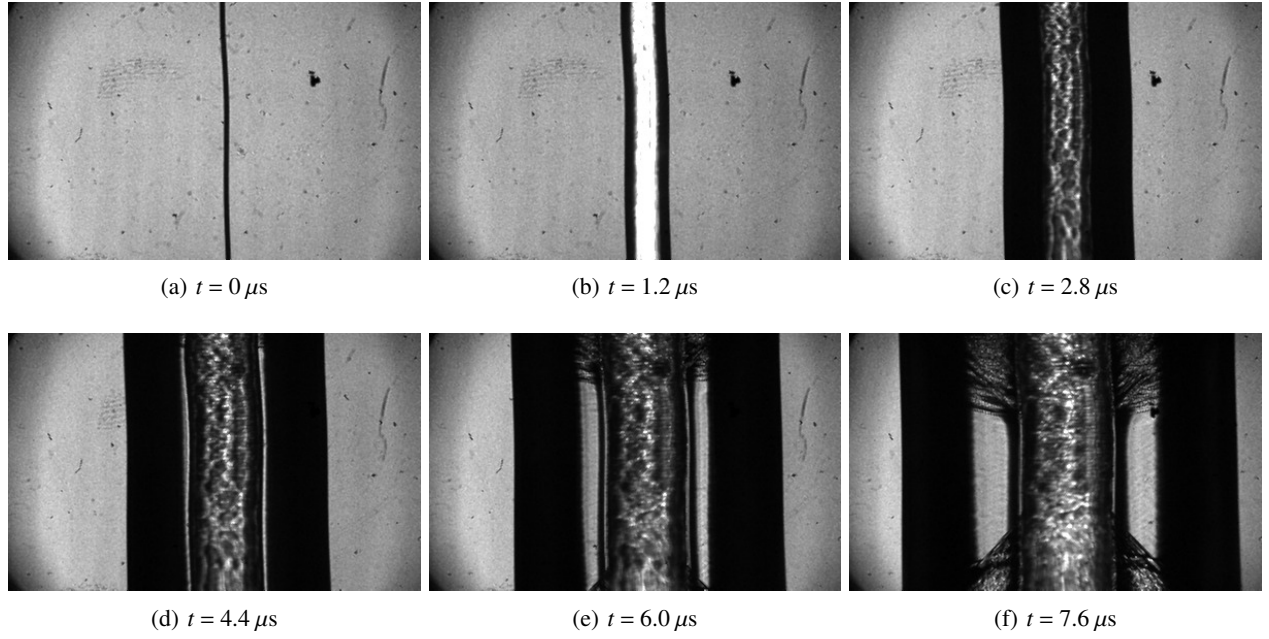


Fig. 16: Frames and relative time of a shock wave generated by a $\varnothing 400 \mu\text{m}$ wire explosion and $v_c(0) = 23 \text{ kV}$ in water.

expansion phase after the explosion is well represented by a constant acceleration, and that Lin's equation (1) might not be applicable in this phase, since it considers a non-constant acceleration instead.

The same process is carried out for each of the 12 single-wire explosions, getting the corresponding initial speed and Mach numbers of the generated shock waves at the first available data points. The results of this analysis are summarized in Figure 18, which shows the initial Mach numbers of all the generated shock waves. Note that the shock waves in air can achieve Mach numbers greater than 20. In water, the achieved Mach numbers are an order of magnitude smaller, although as mentioned before, the corresponding generated pressures are significantly larger than in air.

The process of shock wave generation is highly dependent on the dynamics of the expansion of the wire. For a given wire diameter, a faster current discharge yields a quicker expansion, which in turn translates into a more energetic shock wave. Due to this reason, the dependency of the initial Mach with the initial capacitor voltage can be explained. Increasing the initial voltage also increases the Mach number of the generated shock wave, since the expansion process of the wire happens faster. However, the relationship between the initial Mach number and the size of the wire is rather a more complex physical phenomenon. Increasing the wire size does not necessarily increase the initial Mach number. In fact, Figure 18 shows experimental evidence of the existence of an optimal wire size for efficient shock wave generation in air. This phenomenon is related with the energy partition and it has been previously documented in the literature, as explained in Section II-B. In the context of this thesis, the optimal wire size identified for air explosions is around $\varnothing 400 \mu\text{m}$, whereas for water it has not been found, although $\varnothing 500 \mu\text{m}$ gives the fastest shock.

The physical explanation of this phenomenon involves several factors, such as the electrical-to-mechanical energy transfer, the skin depth effect, the creation of parasitic plasma over the wire, and the influence of the compressibility of the medium as the wire expands. This will be further discussed in Section VI-A.

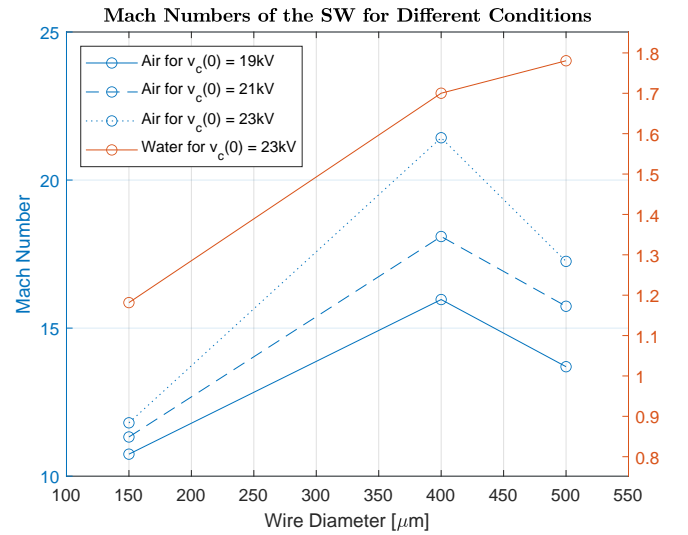


Fig. 18: Initial Mach numbers of the generated shock waves in air and water.

2) *Analysis of the Electrical Waveforms:* This section explains how the PPG behaves electrically during single-wire explosions. The electrical waveforms are studied to develop a method to compute the power and energy supplied to the wires by the PPG. The first task carried out has been to estimate the voltage at the wire (v_2) by means of the voltage at the main electrode (v_1) thanks to the previously found electrical

parameters of the PPG, summarized in Table I. Once the signal of the high-voltage probe measuring the voltage at the main electrode is received in the control room, it needs to be multiplied by 2.50 kV/V to get the proper v_1 accounted for signal attenuation. Since there is only an inductance of $L_3 = 23.3$ nH between v_1 and v_2 , the voltage at the wire will be computed by $v_2 = v_1 - L_3 \frac{di_L}{dt}$. An example of this is given in Figure 19 for a water explosion with $v_c(0) = 21$ kV and $\varnothing 400 \mu\text{m}$. The results show great agreement, especially in the first step at around $6 \mu\text{s}$ and the voltage peak at around $7 \mu\text{s}$. Note that this region is the most critical in terms of finding the electrical energy transferred to the wire, since the time of explosion is associated with a peak in resistive voltage. A great agreement is found for all the studied explosions, validating again the circuit parameters given in Table I.

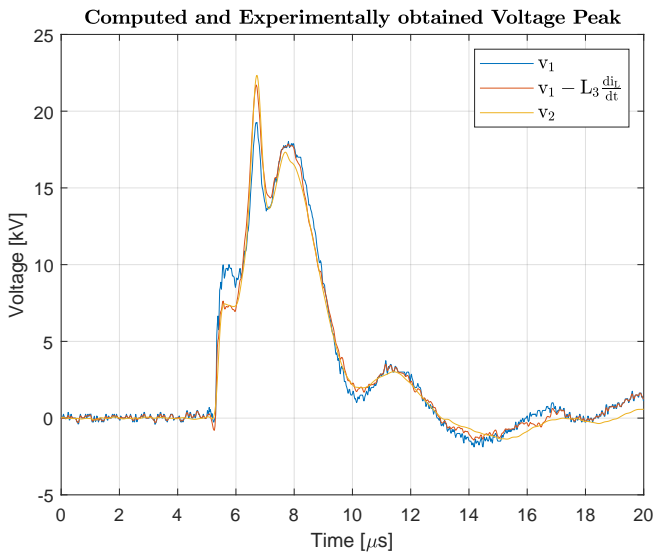


Fig. 19: Computed voltage peak by using the inductance of the main electrode for water $v_c(0) = 21$ kV and $\varnothing 400 \mu\text{m}$ wire.

The explosion of the wire is characterized by two consecutive phase changes, which happen very rapidly. Once the wire is in the gas state, a shock wave is created, and the energy pumped by the PPG is directed to heat the gas, turn it into plasma, and expand the plasma as it energetically feeds the generated shock wave due to this expansion. Therefore, the shock wave is created when the wire turns into a gas state. This instant is considered the time of the explosion t_e , and it comes just after a sudden decrease of the current flowing through the system as the wire starts expanding. This sudden decrease in current yields a peak in the resistive voltage at around the instant t_e . How close this instant is to the peak in electrical power is not yet settled in the literature. However, the peak in power must be located close to this instant, for which we associate t_e with the peaks in both voltage and power for the context of this thesis for the sake of simplification. More information regarding the time-location of these peaks and the instant of generation of the shock wave is given in D. Maler [25].

The voltage v_2 corresponds to the total voltage drop across the wire and it has two contributions: resistive (v_R) and inductive (v_L). The equations to compute resistance and inductance are given in (36) and (37), respectively. These depend on the wire diameter, which in turn depends on time as the wire is expanding. Since the inductive voltage can be computed as $v_L = L_w \frac{di_L}{dt}$, the equation $v_R = v_2 - L_w \frac{di_L}{dt}$ can be used to compute the resistive voltage of the wire. To perform this calculation, the inductance of the wire is considered to be constant and equal to its self-inductance from $t_0 = 0 \mu\text{s}$ until t_e , before the wire changes its phase to gas state and starts expanding abruptly. This assumption is substantiated by the hypothesis that the expansion of the wire prior to transitioning to a gaseous state is relatively small. It allows the computation of v_R from t_0 until t_e , which is crucial to obtain the power and energy transferred by the PPG until the wire is exploded. Naturally, this hypothesis is more valid close to t_0 than to t_e . Table II is included for the values of L_w used in the calculations.

TABLE II: Self-inductances of the employed wires.

Diameter	$\varnothing 150 \mu\text{m}$	$\varnothing 400 \mu\text{m}$	$\varnothing 500 \mu\text{m}$
L_w [nH]	79.5	67.8	65.1

The experimental voltage waveforms are plotted alongside the resistive voltage peaks in Figure 20 for the three wire diameters with initial capacitor voltages of $v_c(0) = 23$ kV in air and water. The currents are plotted in Figure 21 for the same experimental conditions. Note that the larger the diameter, the fewer oscillations after the explosion (i.e. the damping ratio increases). For larger diameters, a greater amount of electrical energy is required to explode the wire, resulting in a slower yet more energetically intense explosion. Typically, explosions occur at a slower pace in water compared to air. Regarding the voltage waveforms, while the total voltage v_2 decreases as the wire size increases, the resistive voltage v_R increases. The difference between v_2 and v_R in the voltage peak is nothing else but the inductive voltage v_L . Since much more energy is needed to explode large wires in comparison to small ones, a much higher electric power needs to be discharged in a relatively similar amount of time t_e . This translates into higher currents and resistive voltages as the wire diameters increase. The inductive voltage will be higher accordingly, with an opposite sign to the resistive voltage. Regarding the currents, note that the first current peak increases significantly in magnitude, while the second peak (restrike) decreases with the wire size. The wire starts expanding after the first current peak, yielding the peak in resistive voltage shortly afterwards.

3) *Electrical Energy Transferred to the Wire:* This section makes use of the previously given electrical waveforms to estimate the electrical energy transferred by the PPG to the wire until the time of the explosion. Once the resistive voltage of the wire v_R and the current flowing through the system i_L are known, the power transferred by the PPG to the wire can be estimated with $P(t) = v_R \cdot i_L$. The transferred electrical energy is given as the integral of the power in time, as shown in equation (48).

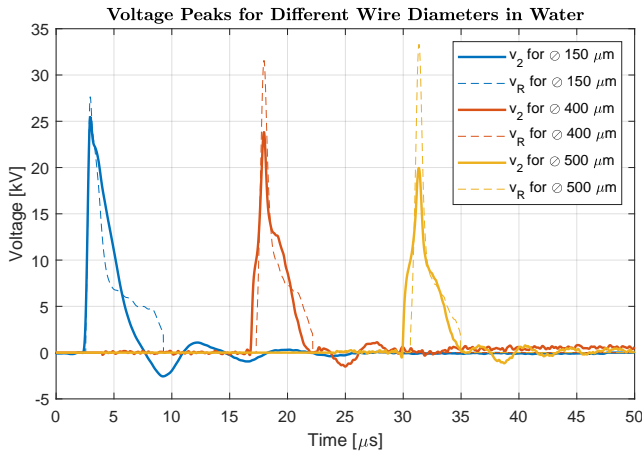
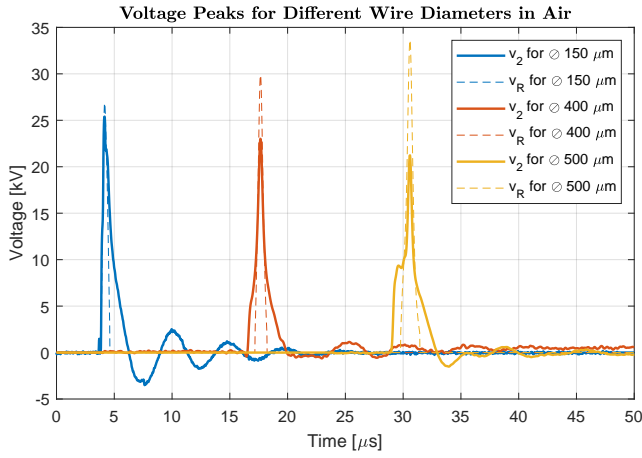


Fig. 20: Experimental voltage peaks at v_2 for air and water explosions with $v_C(0) = 23$ kV.

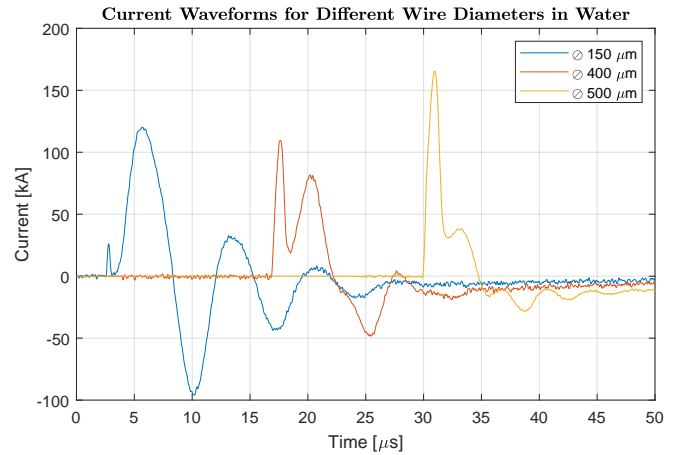
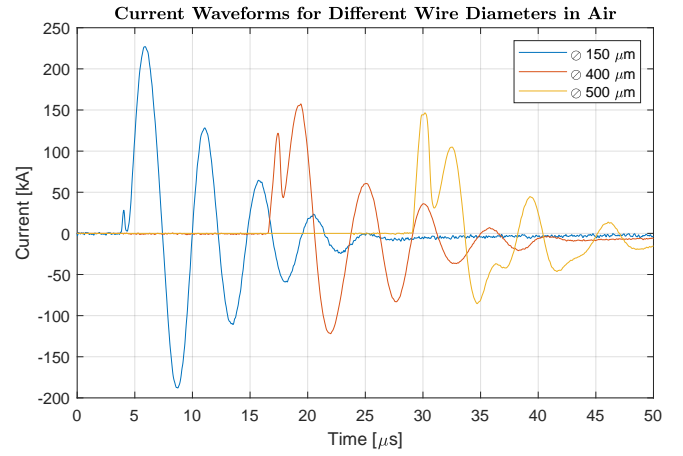


Fig. 21: Experimental current waveforms for air and water explosions with $v_C(0) = 23$ kV.

$$E_E = \int_{t_0}^{t_e} P(t) \cdot dt = \int_{t_0}^{t_e} v_R \cdot i_L \cdot dt \quad (48)$$

Note that the electrical energy is only valid from t_0 until t_e , since the inductance of the wire will change significantly after t_e and the hypotheses made to compute v_R will no longer be valid. The results of performing such calculations are illustrated in Figure 22 for water explosions with $v_C(0) = 23$ kV and different wire sizes. The power magnitude ranges from hundreds to thousands of MW, yielding a clear peak at around the time of the explosion, defined as t_e . Increasing the wire diameter increases the power and electrical energy transferred to the wire until the peak of power. The second derivative of the energy changes sign at t_e , when $\frac{dP}{dt} = 0$ and $\frac{d^2E}{dt^2} = 0$. The total energy up to this instant is considered to be the electrical energy transferred to the wire before the explosion E_E , when the shock wave is detached and the wire turns into plasma. This process can be repeated for all the explosions to obtain the transferred energy for all the studied cases. A summary of these results can be found in Figure 23, showing E_E for all the wire diameters and different initial capacitor voltages.

The insights extracted from Figure 23 are extremely relevant to understand the exploding wire phenomena. On the one hand, the electrical energy transferred to the wire to generate an explosion does not seem to depend on the initial capacitor voltage or the surrounding medium, at least for the studied range of experimental conditions. This indicates a significant degree of independence: the electrical energy required to explode a given wire remains unaffected by extrinsic factors, such as the energy available in the circuit or the surrounding medium. On the other hand, the energy E_E seems to only depend linearly on the square of the wire diameter. For a fixed wire length, the square of the wire diameter and the volume of the wire are proportional, which in turn is proportional to the initial mass of the wire. Therefore, one can say that the required electrical energy to generate an explosion is only linearly proportional to the initial mass of copper contained in the wire, for the studied range of experimental conditions. This constant proportionality factor is defined as K , which describes the slope of the dependency of E_E with the initial volume of the wire, as given in equation (49).

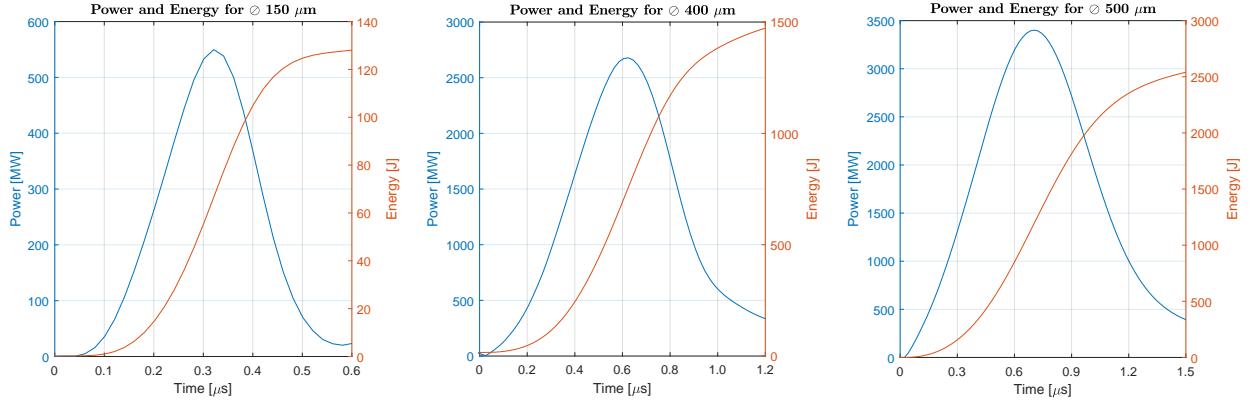


Fig. 22: Power and energy over time for water explosions with $v_c(0) = 23$ kV and different wire diameters.

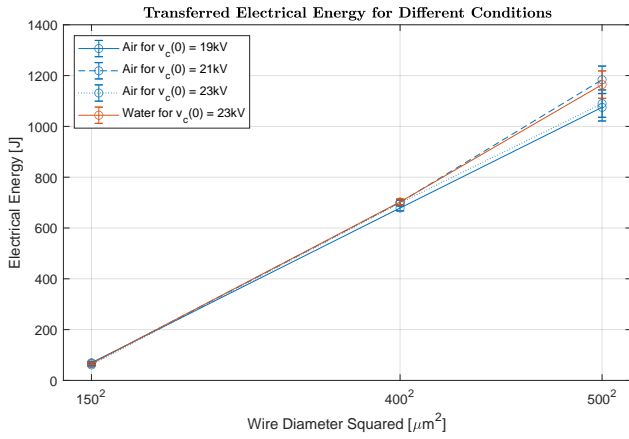


Fig. 23: Transferred electrical energy to the wires until the instant of the explosion.

$$\frac{dE_E}{dV} = K = 99\,100 \text{ J/cm}^3 \quad (49)$$

The transferred electrical energy per unit volume can now be expressed as $e_E = \frac{E_E}{V}$. Since the relationship between E_E and V is known and assumed to be linear, it is also possible to mathematically find the relationship between e_E and V by means of integration. Simple mathematical manipulation makes it possible to arrive at equation (50), where e_0 and V_0 are boundary conditions (taken as the average experimental values for the four explosions with $\varnothing 150 \mu\text{m}$).

$$\begin{aligned} \frac{de_E}{dV} &= \frac{d\left(\frac{E_E}{V}\right)}{dV} = \frac{dE_E \cdot V - E_E \cdot dV}{V^2 dV} = \frac{KV - E_E}{V^2} \\ \frac{de_E}{dV} &= \frac{K}{V} - \frac{e_E}{V} \rightarrow \int_{e_0}^{e_E} \frac{de_E}{K - e_E} = \int_{V_0}^V \frac{dV}{V} \\ \ln\left(\frac{K - e_E}{K - e_0}\right) &= \ln\left(\frac{V_0}{V}\right) \rightarrow K - e_E = \frac{V_0}{V}(K - e_0) \\ e_E &= K - \frac{V_0}{V}(K - e_0) \end{aligned} \quad (50)$$

Equation (50) is plotted alongside the experimental volumetric electrical energy in Figure 24. A very good agreement is found between the experimental results and the given equation. As the volume increases, the volumetric energy e_E tends to a horizontal asymptote defined by K . Therefore, in the studied range of experimental conditions where $\frac{dE_E}{dV}$ is assumed to be constant and equal to K , the maximum possible volumetric energy transferred to the wire is completely determined by the slope $\frac{dE_E}{dV}$. Increasing the wire diameter from $\varnothing 150 \mu\text{m}$ to $\varnothing 400 \mu\text{m}$ significantly increases the volumetric energy transferred to the wire by $\sim 33\%$, while increasing it from $\varnothing 400 \mu\text{m}$ to $\varnothing 500 \mu\text{m}$ only increases it by $\sim 3\%$, although it may strongly affect the dynamics of the wire expansion. The single parameter K , together with equation (50), define how well the PPG behaves in terms of single-wire explosion electrical energy transfer, for which it could be used as design criteria for PPGs with similar applications. Note that changing the wire length does not modify the value of this asymptote.

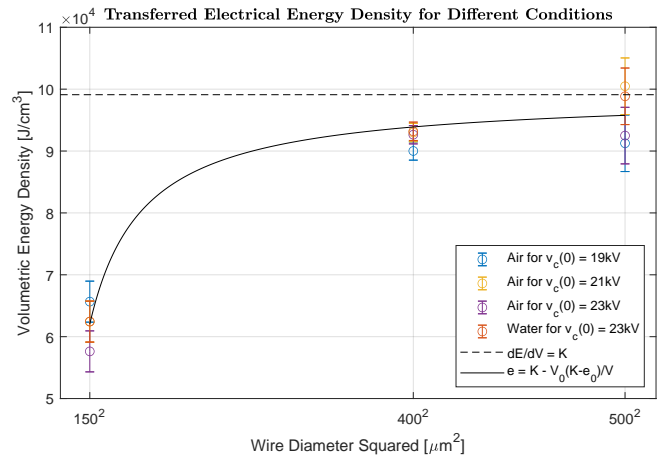


Fig. 24: Transferred volumetric electrical energy to the wires until the instant of the explosion.

These results indicate that it is not desirable to increase the diameter further than $\varnothing 400 \mu\text{m}$ when it comes to transferring electrical energy efficiently, since it does not significantly increase the volumetric electrical energy. Furthermore, side

effects such as the appearance of parasitic plasma or skin depth effect could have a stronger impact on the expansion of the wire as the diameter keeps increasing. The results still do not conclude anything in terms of mechanical energy transferred to the wire, which is analysed in Section V-B4. To finalise, Tables III and IV are included to summarize the electrical results characterizing the explosions in water and air, respectively. Note that v_f is the final voltage in the capacitors after the explosion, which together with the initial voltage v_0 define the available energy transferred to the system $E_a = \frac{1}{2}C(v_0^2 - v_f^2)$. These tables also include the transferred electrical energy and the volumetric electrical energy density.

TABLE III: Electrical results of the water explosions.

Water					
Wire Diameter \varnothing [μm]	Initial Voltage v_0 [kV]	Final Voltage v_f [kV]	Available Energy E_a [J]	Electrical Energy E_E [J]	El. Energy Density e_E [J/cm ³]
150	23	2	2 625	66	62 442
400	23	2	2 625	702	93 190
500	23	2	2 625	1 164	98 845

TABLE IV: Electrical results of the air explosions.

Air					
Wire Diameter \varnothing [μm]	Initial Voltage v_0 [kV]	Final Voltage v_f [kV]	Available Energy E_a [J]	Electrical Energy E_E [J]	El. Energy Density e_E [J/cm ³]
150	19	2	1 785	69	65 661
	21	2	2 185	66	62 434
	23	2	2 625	61	57 624
400	19	2	1 785	678	90 010
	21	2	2 185	701	92 989
	23	2	2 625	698	92 638
500	19	2	1 785	1 075	91 256
	21	2	2 185	1 183	100 474
	23	2	2 625	1 089	92 497

4) Mechanical Energy Transferred to the Shock Wave:

Providing the mechanical energy transferred by the expanding wire to the shock wave has proven to be challenging. The applicability of Lin's equation (1) is limited and not suitable for the explosions carried out in this thesis, as it will be explained in Section VI-B. The alternative of performing MHD simulations is considered outside the scope of this project. Hence, it is necessary to develop a new simplified model to estimate the work done by the wire as it expands. This new model consists of four hypotheses which will be described in the following paragraphs. Thanks to these hypotheses, the force acting inside the expanding wire can be estimated, which is integrated to find the work done by this cylindrical expanding piston. The work done by the expansion of the wire will mainly contribute to compressing the medium during the initial instants of the explosion.

Once the velocity of the advancing shock wave is determined thanks to the HPV-X2 camera, equations (28) and (29) are used to determine the initial velocity of the gases trailing behind it in the air (denoted by u_p). These shock relations also provide the peak pressure obtained behind the shock

wave. Immediately following detachment, the shock wave stays close to the CS (which separates the expanding wire and the surrounding medium). Thus, it is hypothesised that the gases maintain a constant velocity in the short region between the CS and the shock wave during the initial instants of the explosion, before the characteristic expansion following the blast wave begins to influence the system dynamics. Despite the strong temperature and density change across the CS due to the juxtaposition of two gases, under this assumption, the CS aligns its motion with the velocity of the gases trailing the shock wave within the first few nanoseconds following the explosion. Therefore, just after the explosion at time t_e , the wire begins to expand and the shock wave is generated. This expansion is assumed to strongly affect the energy of the generated shock wave over a time duration of $\Delta t \approx t_e$. Due to the hypothesised conditions, the velocity of the shock wave at the end of this Δt is assumed to be u_p .

As a second hypothesis, the CS is set to have a constant acceleration of approximately $a = \frac{\Delta u}{\Delta t} = \frac{u_p}{t_e}$ as the wire is expanding during Δt following from t_e . This would imply that the kinematics of the CS follow $v(t) = \frac{u_p}{t_e}t$ and $r(t) = \frac{1}{2}\frac{u_p}{t_e}t^2$ for its speed and radial position, respectively. After $\Delta t \approx t_e$, both the shock wave and CS would not suffer such a strong acceleration, and the CS would stop having a strong influence on the shock wave. To validate this second hypothesis, the radial position of the shock wave is captured using the HPV-X2 camera and plotted in Figure 25. This is done for air with a $\varnothing 500 \mu\text{m}$ wire at a capacitor initial voltage of $v_C(0) = 19 \text{ kV}$, since it is the slowest explosion carried out with $t_e = 880 \text{ ns}$. Note that t_e is extracted from the electrical waveforms and it has an experimental error of $\pm 20 \text{ ns}$. The experimental results show a hypothesised radial position of the CS with the expression $r(t) = \frac{1}{2}\frac{u_p}{t_e}t^2$ is behind the position of the shock wave. Furthermore, the speed of the CS at the end of Δt is the speed of the particles u_p behind the shock wave at that instant. After Δt , the behaviour of the shock wave changes, since the CS stops having a strong influence on it.

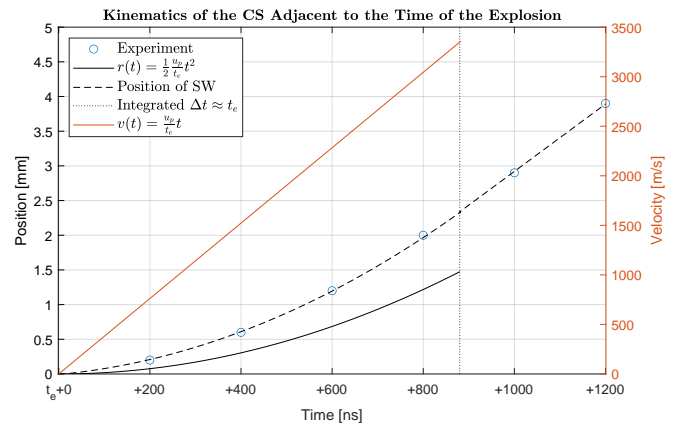


Fig. 25: Experimental and estimated kinematics adjacent to the time of the explosion for the CS in air with $v_C(0) = 19 \text{ kV}$ and $\varnothing 500 \mu\text{m}$.

As a third hypothesis, the acceleration inside the wire is considered to increase radially in a linear way, having a maximum on the surface. This yields $a(r) = \frac{u_p}{t_e} \frac{r}{R}$, where R is the final position of the CS when it stops influencing the shock wave, which corresponds to a volume of the wire at the time $t_e + \Delta t$, given as $V_f = \pi R^2 l$. This third hypothesis is not intrinsically validated, although it provides the necessary framework to obtain good-quality results in terms of mechanical energy. The mass of the wire will remain constant as it expands, being $M = \rho_{cu} V_i$, where ρ_{cu} is the density of solid copper and $V_i = \pi(D/2)^2 l$ is the initial volume of the wire. A fourth hypothesis is made to obtain the mass distribution of the wire. At the final CS position, the wire is discretized in concentric differential cylinders, yielding the differential mass distribution given in equation (51).

$$dm = \frac{M}{V_f} 2\pi l r dr \quad (51)$$

This differential mass distribution will be under radial acceleration. In other words, a non-linear radial force is expanding the wire until the CS gets to $r(\Delta t) = R$ and $v(\Delta t) = u_p$, where $\Delta t \approx t_e$. The expression for this force for the postulated hypotheses is given in equation (52).

$$F(r) = \int_0^r dF = \int_0^r dm \cdot a(r) = \int_0^r \frac{M}{V_f} \frac{2\pi l u_p}{t_e R} r^2 dr \quad (52)$$

This force can now be integrated over the radial direction to get the work done by the force as the wire expands, as shown in equation (53). After integration, a simple expression is obtained for the work done by the expanding wire as given in equation (54).

$$W = \int_0^R F(r) dr = \int_0^R \left(\int_0^r \frac{M}{V_f} \frac{2\pi l u_p}{t_e R} r^2 dr \right) dr \quad (53)$$

$$W = \frac{1}{6} \rho_{cu} V_i \frac{u_p}{t_e} R \quad (54)$$

This last semi-analytical expression provides an estimation of the work done by the expanding wire under the aforementioned hypothesis. The work is proportional to the initial mass of copper, the acceleration of the CS, and the radial position of the CS when it stops influencing the shock wave. All this work is assumed to be transferred to the initial mechanical energy of the shock wave, thus $W = E_M$. How properly are the effects of energy loss, the current skin depth and parasitic plasma are considered in this calculation is still an open question. Even though not considering these effects explicitly in equation (53), the acceleration of the CS is computed using $a = \frac{u_p}{t_e}$, which in turn are the actual experimental parameters implicitly containing real effects. Nonetheless, this simplified model is expected to give slightly higher values than in the actual explosion. This approach is only valid for air since the small compressibility of water also plays a role in the expansion of the wire, which would need to exercise extra

work to compress the medium. To finalise, Tables V and VI are included to summarize the mechanical results characterizing the explosions in water and air, respectively. These include the initial Mach number of the generated shock wave, the peak pressure, the estimated mechanical energy, the efficiency of electrical-to-mechanical energy conversion, and the time to explode.

TABLE V: Mechanical results of the water explosions.

Water						
Wire Diameter \varnothing [μm]	Initial Voltage v_0 [kV]	Initial Mach M_0	Peak Pressure P_0 [kbar]	Mec. Energy E_M [J]	Energy Efficiency [%]	Time to Explode t_e [ns]
150	23	1.18	2.607	-	-	400
400	23	1.70	14.812	-	-	600
500	23	1.78	17.368	-	-	680

TABLE VI: Mechanical results of the air explosions.

Air						
Wire Diameter \varnothing [μm]	Initial Voltage v_0 [kV]	Initial Mach M_0	Peak Pressure P_0 [kbar]	Mec. Energy E_M [J]	Energy Efficiency [%]	Time to Explode t_e [ns]
150	19	10.74	0.133	8.7	12.5	240
	21	11.32	0.154	9.8	14.7	220
	23	11.80	0.165	10.9	17.9	180
400	19	15.97	0.301	132.6	19.5	560
	21	18.09	0.387	169.5	24.2	520
	23	21.43	0.543	236.7	33.9	460
500	19	13.70	0.222	150.6	14.0	880
	21	15.74	0.293	199.6	16.9	760
	23	17.25	0.352	239.0	21.9	720

5) *Electrical-to-Mechanical Energy Conversion*: Once the electrical energy transferred to the wire and the initial mechanical energy of the generated shock waves have been determined, it is crucial to bond both processes to understand how efficiently the PPG converts from electrical to mechanical energy. Note that these efficiencies are given in Table VI for air, being E_M/E_E expressed as a percentage, and ranging between 12% and 34%. The efficiency increases as the initial capacitor voltage increases. This effect is expected, since a larger capacitor voltage produces a faster explosion and increases the speed of the expansion, strongly affecting the generated shock wave and its initial Mach number. The maximum efficiency is found to be in the $\varnothing 400 \mu\text{m}$ wire in all cases, for any given initial capacitor voltage. Therefore, while equation (54) may not provide the exact value of the transferred mechanical energy, it shows consistency in the optimal voltage and wire diameter for maximizing energy transfer efficiency.

On the other hand, Table VI also shows that the transferred mechanical energy E_M increases with the wire diameter. This might look to be in contradiction with the results given in Figure 18, where a clear decrease in Mach number can be observed for the largest diameter in air. However, one must consider that the Mach number of the moving shock wave is directly proportional to the pressure ratio along the shock, as given in equation (28). In other words, the initial Mach number

is directly proportional to the pressure peak, and the pressure peak is in turn proportional to the volumetric mechanical energy density.

To exemplify this, Figure 26 is included to compare the mechanical energy and the volumetric mechanical energy density of the generated shock waves in air, with respect to the corresponding transferred electrical energies until the time of the explosions. Note that the volumetric mechanical energy uses the initial volume of the wires V_i as a reference, being $e_M = E_M/V_i$. It is possible to observe that, as the electrical energy transferred to the wire increases, the mechanical energy transferred to the shock wave also increases. This effect is much more significant going from $\varnothing 150 \mu\text{m}$ to $\varnothing 400 \mu\text{m}$, than going from $\varnothing 400 \mu\text{m}$ to $\varnothing 500 \mu\text{m}$. Regarding the volumetric mechanical energy density (proportional to the pressure peak and generated Mach number), it is possible to observe a clear peak in $\varnothing 400 \mu\text{m}$ in all cases. This shows that equation (54) not only is consistent with the maximum energy transfer efficiency, but also with the wire diameter that produces the maximum pressure peak and the highest Mach number. To summarize, increasing the transferred electrical energy does increase the mechanical energy of the shock wave, although it does not necessarily increase the pressure peak and initial Mach number, which in fact have a maximum at around $\varnothing 400 \mu\text{m}$ for the studied PPG.

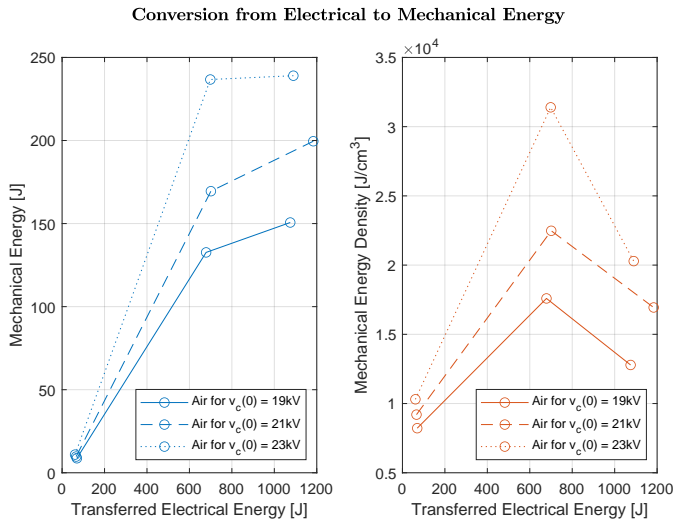


Fig. 26: Mechanical energy and volumetric mechanical energy density of the generated shock wave in front of the transferred electrical energy for explosions in air.

VI. DISCUSSION

The present section discusses the obtained results, emphasizing the existence of an optimal wire diameter and the applicability of theoretical and CFD models for single-wire explosions.

A. Existence of an Optimal Wire Diameter

Section V shows experimentally that an optimal wire diameter exists for single-wire explosions in air. It has not been shown for explosions in water, although it is expected to have a similar behaviour for larger wire diameters. This phenomenon is expected as it has been in the literature since 1958, when Bennett first described this energy partition during exploding wires, as explained in Section II-B. This non-linearity can be explained physically from different points of view.

The first explanation can implicitly be extracted from Figures 24 and 26. On the one hand, the volumetric electrical energy density has been shown to have asymptotic behaviour with the wire volume, with a horizontal asymptote corresponding to the value of the slope dE_E/dV . Pragmatically, this implies that increasing the wire diameter more than $\varnothing 400 \mu\text{m}$ does not increase the volumetric electrical energy density transferred to the wire significantly, for the studied PPG. On the other hand, increasing the transferred electrical energy does not increase the mechanical energy of the generated shock wave significantly for higher diameters. In other words: increasing the initial wire diameter more than $\varnothing 400 \mu\text{m}$ does not significantly increase the transferred electrical nor mechanical energies, although it increases the wire volume quadratically. This yields a decrease in the volumetric mechanical energy density for large diameters, which in turn is proportional to the peak pressure behind the shock and its initial Mach number, defining this optimal diameter.

A second explanation is related to the skin depth effect. Alternating current in a conductor induces a changing magnetic field. This variation is due to the constant shift in the magnitude and direction of the current itself. As predicted by Faraday's law of induction, this fluctuating magnetic field induces an opposing current within the conductor. These induced currents are called eddy currents. Eddy currents generate their own magnetic field that opposes the original magnetic field. This opposition is strongest in the centre of the conductor, forcing the current to flow near the surface, a phenomenon known as the skin effect. The skin depth δ refers to the distance at which the current density reaches approximately 37% of its value at the surface of the wire. A formula to estimate this distance δ is found in Reto B. Keller [26] and given in equation (55).

$$\delta = \sqrt{\frac{\rho}{\pi f_0 \mu_r \mu_0}}. \quad (55)$$

Here, $\rho = 1.678 \mu\Omega\cdot\text{cm}$ is the resistivity of copper at standard temperature, $\mu_r = 0.999991$ is the relative magnetic permeability of copper, $\mu_0 = 4\pi \cdot 10^{-5} \text{ T}\cdot\text{cm/A}$ is the magnetic permeability of vacuum, and f_0 is the frequency of the current oscillations, computed in Section V-A2 as $f_0 = 181 \text{ kHz}$. For the studied PPG and copper wire explosions, the skin depth has a value of $\delta \approx 153 \mu\text{m}$, which means that this effect starts being significant for wire diameters larger than $D > 300 \mu\text{m}$. This implies a non-uniform distribution of the current within the wire, which is firstly sublimated on its surface rather than its centre,

strongly affecting the dynamics of the wire expansion and the initial energy of the generated shock wave. With currents concentrating near the surface due to the skin effect, the intense heating can lead to the emission of electrons and the creation of a plasma sheath surrounding the conductor even before the time of the explosion (and sudden expansion). This plasma sheath, also alters the dynamics of the current distribution and can significantly affect the conductor's behaviour, as explained in Gonzalo Rodríguez Prieto et al. [14].

A third explanation considers an additional source of plasma, known as parasitic plasma, which can manifest particularly during explosions in the air. This phenomenon is often attributed to high-frequency electrical currents. When high-frequency alternating currents flow through a conductor, they can ionize the surrounding gases, resulting in the formation of plasma affecting the dynamics of the explosion.

The difference in the optimal wire diameter between air and water can be associated with three factors: (1) the skin depth effect creating non-uniform explosions; (2) the creation of parasitic plasma over the wire in air explosions; and (3) the small compressibility of water. As the wire expands in water, it needs to exert more energy compressing the medium compared to air, which in turn will decrease the amount of work transferred into kinetic energy, but increase the generated peak pressure. Therefore, the generated shock waves are significantly stronger and slower in water. Smaller wire expansions create higher pressures, which affect the optimal wire diameter.

B. Applicability of Theoretical and CFD Models

This section studies the applicability of Lin's equation (1), also known as Sedov's equation, to properly characterize the single-wire explosions carried out in this thesis. This equation in the given form is only valid for an ideal diatomic gas and can be solved directly for the radial position of the shock wave $R(t)$ in time, given an initial energy per unit length deposited instantaneously. Further details are given in Section II-A.

For the sake of comparison, CFD simulations are included and compared with the experimental results and Lin's model. These simulations are carried out employing an in-house code provided by Senior Prof. Nicholas Apazidis, based on an Artificial Upstream Flux Vector Splitting (AUFVS) scheme. This method solves the differential conservation equations defined in (17), (18) and (19) considering the ideal gas law to close the system. The method was proposed by M. Sun and K. Takayama [27] in 2003, and it is a robust upwind scheme proven to work for inviscid compressible flow problems. The employed mesh is two-dimensional consisting of triangular elements. A zoomed illustration of the used triangular mesh around a $\varnothing 150 \mu\text{m}$ wire is included in Figure 27. Only this wire diameter is simulated. The employed mesh contains 13 089 triangles with a mean quality factor of 0.9124 (topped at 1), taking the aspect ratio of the triangles as a quality reference. This aspect ratio is computed as a normalized

measure of the triangle's area relative to its perimeter, being equal to one for an equilateral triangle.

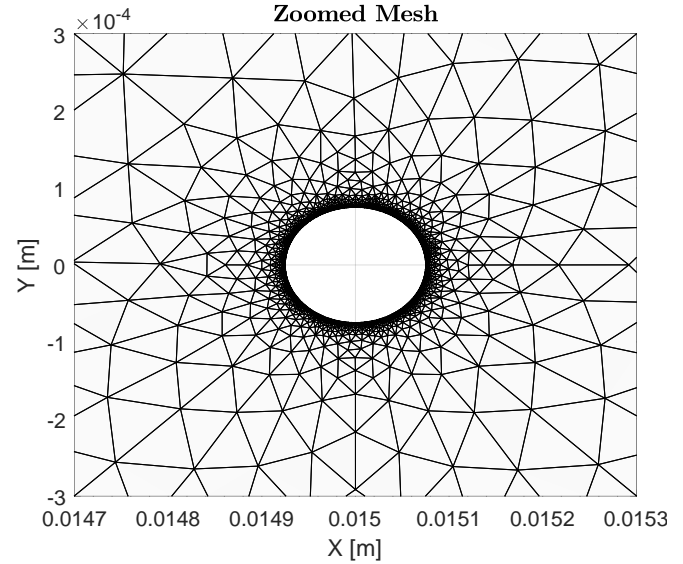


Fig. 27: Zoomed illustration of the employed triangular mesh for a $\varnothing 150 \mu\text{m}$ wire.

The simulations are carried out for different initial mechanical energies, which are estimated by adding an initial pressure boundary condition applied to an area equivalent to the initial cross-section of the wire. This idea comes from the energy conservation equation (22), which can be modified in the following way $\frac{\gamma}{\gamma-1}(p/\rho) + u^2/2 = C$, where C is constant as given in Anderson [20] for a calorically perfect gas. Instants before the explosion, the released mechanical energy per unit volume will be equivalent to $e_M = \frac{\gamma}{\gamma-1}p$, which sets the pressure applied as an initial boundary condition. Figure 28 provides an example of one of these CFD simulations, showing two frames separated by $3 \mu\text{s}$ of an evolving shock wave generated by an explosion of a $\varnothing 150 \mu\text{m}$ wire with a mechanical energy of 10 J. After the simulations, a post-processing algorithm is used to find the radial position of the shock waves in time.

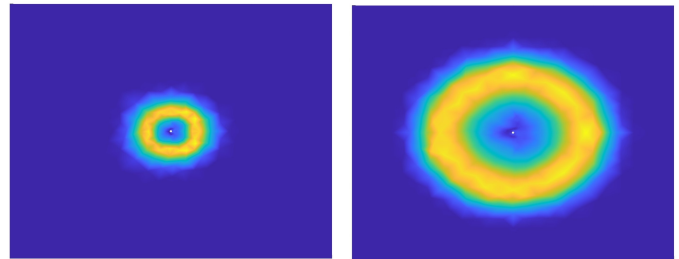


Fig. 28: Normalized total velocity from a CFD simulation of a $\varnothing 150 \mu\text{m}$ wire with $E_M = 10 \text{ J}$ at two different times separated by $3 \mu\text{s}$ for a domain measuring 20 mm by 20 mm.

The results from applying both Lin's equation and the CFD model are compared with the experiment's results in Figure 29, which shows the radial position and speed of the shock wave. This is done for an explosion with a wire of $\varnothing 150 \mu\text{m}$ and an initial capacitor voltage of 19 kV. Based on the data presented in Table VI, the explosion under consideration contains a mechanical energy of roughly 8.7 J, constituting approximately 12.5% of the transferred electrical energy, estimated at about 69.6 J. Lin's analytical solution, represented graphically, assumes a total mechanical energy of 10 J to be over-conservative. Meanwhile, the numerical solutions obtained via CFD simulations are shown for mechanical energies of both 10 J and 50 J. Notably, a good agreement is observed between Lin's analytical solution and the CFD model when the mechanical energy is set at 10 J, thus validating the accuracy of the numerical computations. Nonetheless, the experiments seem to present completely different behaviour than the analytical and numerical models. Increasing the energy of the numerical solution to 50 J does not match the experimental solution either.

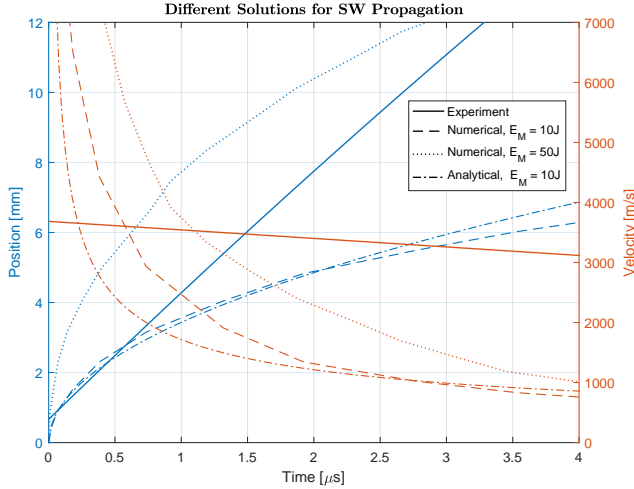


Fig. 29: Comparison between experimental, numerical and analytical approaches for the radial position and speed of the shock wave.

The discrepancy can be justified in different ways. Initially, both the analytical and numerical models assume an instantaneous energy release. However, this assumption remains valid only at radial distances sufficiently distant from the wire, and therefore at times long after the explosion. As detailed in Section II-A, Sakurai establishes this minimum distance to be significantly greater than the radius of a cylinder of air with a mass equivalent to the explosive material in the wire (denoted by \bar{R}). For a copper wire with a diameter of $\varnothing 150 \mu\text{m}$, this equivalent distance yields $\bar{R} = 0.64 \text{ cm}$. Conversely, if the distance exceeds a certain maximum threshold, the relationship between the travelled distance R^2 and time t , as defined in Lin's equation, no longer holds true. Sakurai defines this upper limit with the distance R_0 , given in equation (3) and resulting in $R_0 = 1.62 \text{ cm}$. The theoretical framework remains applicable only in the region $R \gg \bar{R}$ and $R \leq 0.4R_0$, yet for $\bar{R} = 0.64 \text{ cm}$ and $R_0 = 1.62 \text{ cm}$ such conditions do not exist in the studied

explosions. This justifies that the analytical model can not be applied to characterize the studied shock waves. Furthermore, both the analytical and numerical models do not consider the dynamics of the expanding wire, which strongly affects the shock wave via aggregation of compression waves behind the shock front.

On the other hand, the CFD solver does not consider the coupling between the mechanics of the fluid and electromagnetic effects. Such a coupling is relevant to being able to characterize properly the behaviour of the flow, as explained in Section III-E. The current flowing through the plasma channel creates a significant magnetic field that affects the shock wave even after detachment, creating a highly transient and non-linear process that needs to be simulated with a more advanced model, such as the MHD system provided in equations (39), (40), (41) and (42).

VII. CONCLUSION

This section summarizes the performed work and gives a proposal for future work following this project.

A. Summary

This project aims to determine the optimized PPG parameters and initial conditions for the most efficient electrical-to-mechanical energy transformation during single-wire explosions. The first task carried out has been a literature review, where three different topics have been discussed: (1) the search for a self-similar solution applicable to exploding blast waves, where Lin's equation plays a pivotal role in describing cylindrical explosions; (2) the energy partition during single-wire explosions, mentioning the existence of optimal wire diameters; and (3) the importance of the electrical circuit behaviour which is strongly coupled to the properties of the generated shock wave.

The second task has been to understand and summarize the relevant theoretical background of the single-wire explosions. Here, a multi-disciplinary analysis has been carried out by linking electrical systems, fluid mechanics and visualization techniques. An electrical RLC model is proposed to characterize the PPG, and the conservation equations of the fluid are analysed to derive jump relations for the moving shock waves in air and water. Thereupon, the third task has been to describe the methods employed during the experiments. A detailed description of the PPG, the system connections and the optical setup is given along with descriptions of the involved hardware and how to operate the laboratory. An explosion procedure is given, including safety considerations for secure laboratory operation.

The fourth task has been to determine the electrical parameters of the PPG by means of experimental measurements in short-circuit experiments. This has been done by dividing the circuit into four sections: voltage source, spark gap, main electrode and test chamber. Each section is associated with either a capacitance, resistance, inductance or a combination

of them. A simplified RLC model is applied, comparing the experimental waveforms with the analytical solution. To further verify the results, the circuit is solved numerically using a SPICE simulator. The resistance of the spark-gap is time-dependent, and it has been modelled as a function of the initial capacitor voltage and time. This combined approach has provided the electrical parameters of the circuit, summarized in Table I, which in turn provide good agreement with the experimental results when plotting the corresponding waveforms. The fifth task has been to calibrate the RC and find relations between the different high-voltage probes employed in the experiments. This has been done in parallel while determining the electrical parameters of the PPG, yielding $\beta_{RC} = 696.69 \frac{\text{A}}{\text{V}}$ for the RC and 2.5 kV/V for the relation of the high-voltage probe signal in the test room measured from the control room.

The sixth task has been to carry out a systematic single-wire explosion campaign, exploding three different wire sizes of $\varnothing 150 \mu\text{m}$, $\varnothing 400 \mu\text{m}$ and $\varnothing 500 \mu\text{m}$ for initial capacitor voltages of 19 kV, 21 kV and 23 kV in air. Only the initial capacitor voltage of 23 kV is exploded in water, yielding a total number of 12 explosions (9 in air and 3 in water). The radial position of the generated shock waves is recorded with the high-speed camera, yielding the evolution of the Mach number of the shock waves in time. By using this Mach number in the moving shock waves relations, it has been possible to estimate the peak pressure of the explosions, which is in the order of hundreds of bar in air, and tens of kbar in water (or approximately 50 times stronger in water than in air). Furthermore, out of the three diameters tested, the wire diameter of $\varnothing 400 \mu\text{m}$ is found to give the highest peak pressure and initial Mach number in air.

The seventh task has consisted of estimating the transferred electrical energy to the wire until the moment of explosions, and the initial mechanical energy of the generated shock waves. Regarding the electrical energy, this has been done by studying the recorded electrical waveforms by the RC and high-voltage probes during the explosions. By using the self-inductance of the wire and its resistive voltage, peak powers in the order of 3 500 MW have been estimated close to the instant of the explosion (when the wire starts expanding abruptly). The total transferred electrical energy has been estimated by integrating this power in time, showing linear behaviour with the initial volume of the wire, independently of the medium and initial capacitor voltage. This linear behaviour is characterized by the slope $\frac{dE_E}{dV} = K = 99\,100 \text{ J/cm}^3$, which in turn also defines the value of an horizontal asymptote in the volumetric electrical energy density as a function of the initial volume of the wire. Pragmatically, this means that increasing the wire diameter too much does not give a significant increase in the transferred electrical energy per unit volume, with $\varnothing 400 \mu\text{m}$ being the wire size at which approximately 95% of the maximum energy density can be transferred. Regarding the transferred mechanical energy, a new semi-analytical model is proposed to estimate the work done by the wire during its expansion. This work is proportional to the initial mass of copper, the acceleration of the CS, and the radial position of the CS when it stops influencing significantly the shock wave.

The eighth task has been to study the electrical-to-mechanical energy transfer efficiency. This has been done only for air, since the proposed model to estimate the mechanical energy of the shock waves is not applicable for water. The least efficient situation has been found for a $\varnothing 150 \mu\text{m}$ wire at initial capacitor voltage of 19 kV, converting only 12.5% of the transferred electrical energy to mechanical energy. The most optimal situation has been found for a $\varnothing 400 \mu\text{m}$ wire at initial capacitor voltage of 23 kV, having an efficiency of 33.9%. Overall, increasing the initial capacitor voltage always increases this efficiency, since it yields a faster explosion with a wire expanding quicker. The proposed model for the mechanical energy has shown to be consistent with the maximum energy transfer efficiency, and the wire diameter that produces the maximum pressure peak and the highest Mach number.

The ninth task has been to discuss these results, justifying the existence of an optimal wire diameter by means of the electrical-to-mechanical energy transfer efficiency, the skin depth effect that starts being significant at wire diameters larger than $D > 300 \mu\text{m}$, and the parasitic plasma appearing over the wire before the abrupt expansion. Furthermore, the applicability of Lin's analytical equation and CFD models to characterize the wire explosions has been studied. The CFD solver consists of a two-dimensional in-house code based on a AUFS scheme for inviscid compressible flow. The discussion explains that the employed models are not applicable to characterize the studied experiments.

To conclude, the tenth task has been to create this summary and write the proposal for future work given in the following Section VII-B. Overall, all the objectives of the project presented in Section I-C have been successfully accomplished. The main research question has been answered by means of a multidisciplinary analysis involving experimentation, application of theoretical models and numerical approaches.

B. Future Work

This section discusses potential future work. To better understand the single-wire explosions, the main refinement point is to improve the calculation of the electrical and mechanical energies. A more complex MHD numerical simulation is needed, coupling the electrical circuit, the wire expansion, and the effect of electromagnetic fields on the shock wave generation. This will enable a comprehensive understanding of how electromagnetic forces influence the behaviour of the exploding wire and the resulting shock waves in the surrounding fluid. Implementing MHD simulations will not only refine the predictive capabilities of the models but also offer deeper insights into the underlying physics governing single-wire explosions. Similar work has been done before by Kyoung-Jae Chung et al. [16].

Following from the future applications defined in Section I-B, the PPG can be used in a wide range of applications. There are short-term plans to use the same PPG for shock-focusing in different mediums. This work will allow for the generation of very extreme conditions in different materials, which can

have major scientific relevance. Additionally, there are plans to utilize the PPG to investigate how nanofibers behave under extreme tension and compression conditions. This research can exhibit how nanofibers respond to stress, deformations, and external forces, which is crucial for applications such as nanocomposites, nanoelectronics, and biomedical devices. In summary, the PPG proves to be a crucial tool with wide-ranging applications across various fields. This investigation on single-wire explosions marks the beginning of its potential impact.

ACKNOWLEDGMENTS

The author of this thesis wants to thank Prof. Michael Liverts and Post-doc. Sebastián Rojas Mata for their supervision and guidance throughout the project. Gratitude is also extended to Senior Prof. Nicholas Apazidis for providing the CFD code and research guidance. A special thanks to Ph.D. Candidates Sourabh Bhardwaj and Xinyi Wei for the nourishing discussions and provided expertise. Finally, thanks to the family, friends and colleagues who have supported the author throughout the realisation of this project.

REFERENCES

- [1] SV Lebedev, A Frank, and DD Ryutov. “Exploring astrophysics-relevant magnetohydrodynamics with pulsed-power laboratory facilities”. In: *Reviews of Modern Physics* 91.2 (2019), p. 025002.
- [2] M Keith Matzen et al. “Pulsed-power-driven high energy density physics and inertial confinement fusion research”. In: *Physics of Plasmas* 12.5 (2005).
- [3] Michael Liverts and Nicholas Apazidis. “Limiting temperatures of spherical shock wave implosion”. In: *Physical review letters* 116.1 (2016), p. 014501.
- [4] D Yanuka, S Theocharous, and SN Bland. “Pulsed power driven cylindrical wire array explosions in different media”. In: *Physics of Plasmas* 26.12 (2019).
- [5] Hidenori Akiyama et al. “Industrial applications of pulsed power technology”. In: *IEEE Transactions on Dielectrics and Electrical insulation* 14.5 (2007), pp. 1051–1064.
- [6] Shao-Chi Lin. “Cylindrical shock waves produced by instantaneous energy release”. In: *Journal of Applied Physics* 25.1 (1954), pp. 54–57.
- [7] Geoffrey Ingram Taylor. “The formation of a blast wave by a very intense explosion I. Theoretical discussion”. In: *Proceedings of the Royal Society of London. Series A. Mathematical and Physical Sciences* 201.1065 (1950), pp. 159–174.
- [8] FD Bennett. “Cylindrical shock waves from exploding wires”. In: *The Physics of Fluids* 1.4 (1958), pp. 347–352.
- [9] Koichi Oshima. “Blast waves produced by exploding wires”. In: *Exploding Wires: Volume 2 Proceedings of the Second Conference on the Exploding Wire Phenomenon*. Springer. 1962, pp. 159–174.
- [10] FD Bennett and DD Shear. “Shock waves from exploding wires at low ambient densities”. In: *Exploding Wires: Volume 2 Proceedings of the Second Conference on the Exploding Wire Phenomenon*. Springer. 1962, pp. 181–194.
- [11] Akira Sakurai. *Blast wave theory*. Mathematics Research Center, United States Army, University of Wisconsin, 1964.
- [12] FD Bennett and ARMY BALLISTIC RESEARCH LAB ABERDEEN PROVING GROUND MD. “Energy partition in the exploding wire phenomenon”. In: *Phys. Fluids* 1.6 (1958).
- [13] PV Phung and DO Miles. “Skin effect in exploding-wire physics”. In: *Journal of Applied Physics* 46.10 (1975), pp. 4487–4492.
- [14] Gonzalo Rodríguez Prieto, Luis Bilbao, and Malena Milanese. “Temporal distribution of the electrical energy on an exploding wire”. In: *Laser and Particle Beams* 34.2 (2016), pp. 263–269.
- [15] Qing Zhou et al. “Effect of circuit parameters and wire properties on exploding a copper wire in water”. In: *IEEE Transactions on Plasma Science* 39.7 (2011), pp. 1606–1612.
- [16] Kyoung-Jae Chung et al. “Numerical model for electrical explosion of copper wires in water”. In: *Journal of Applied Physics* 120.20 (2016).
- [17] Guofeng Yin et al. “Numerical investigation of shock wave characteristics at microsecond underwater electrical explosion of Cu wires”. In: *Journal of Physics D: Applied Physics* 52.37 (2019), p. 374002.
- [18] A. Agarwal and J.H. Lang. *Foundations of Analog and Digital Electronic Circuits*. Materials 3e North American Edition w/Online Testing. Elsevier, Incorporated, 2005. ISBN: 9781856177436. URL: <https://books.google.se/books?id=opwwlQEACAAJ>.
- [19] Gary S Settles. *Schlieren and shadowgraph techniques: visualizing phenomena in transparent media*. Springer Science & Business Media, 2001.
- [20] John D Anderson. *Modern Compressible Flow With Historical Perspective 3rd Ed*. McGraw Hill, 2003.
- [21] Sadi Ridah. “Shock waves in water”. In: *Journal of applied physics* 64.1 (1988), pp. 152–158.
- [22] David A Ward and J La T Exon. “Using Rogowski coils for transient current measurements”. In: *Engineering Science & Education Journal* 2.3 (1993), pp. 105–113.
- [23] Sivana M Torres, Maria N D’Orazio, and Michael J Hargather. “Focus enhancement in long schlieren imaging systems using corrector lenses”. In: *Applied Optics* 62.29 (2023), pp. 7744–7754.
- [24] *LTspice Simulator*. Analog Devices. URL: <https://www.analog.com/en/resources/design-tools-and-calculators/ltspice-simulator.html> (visited on 04/23/2024).
- [25] D Maler et al. “Addressing the critical parameters for overdamped underwater electrical explosion of wire”. In: *Physics of Plasmas* 29.10 (2022).
- [26] Reto B Keller. *Design for Electromagnetic Compatibility - In a Nutshell: Theory and Practice*. Springer Nature, 2023.
- [27] M Sun and K Takayama. “An artificially upstream flux vector splitting scheme for the Euler equations”. In: *Journal of Computational Physics* 189.1 (2003), pp. 305–329.

